A Causal Network Analysis of Neuromodulation in the Cortico-Subcortical Limbic Network

Shaoyu Qiao[1], Kevin A. Brown[1], J. Isaac Sedillo[1], Breonna Ferrentino[1], and Bijan Pesaran[1,2,3,4,5,*]

[1]Center for Neural Science, New York University, New York, NY 10003
[2]Neuroscience Institute, New York University Langone Health, New York, NY 10016
[3]Department of Neurology, New York University Langone Health, New York, NY 10016
[4]Senior author
[5]Lead contact
*Correspondence: bijan@nyu.edu (B.P.)

Word counts (150 limit)	
Summary	150

Character counts with spaces	
Introduction	5,680
Results	17,179
Discussion	14,461
Main Figure Legends	8,804
Total	46,124

Figure counts	
Main Figures	5
Supplemental Figures	6

Table counts	
Main Tables	0
Supplemental Tables	2

33 **Highlights**

34 - Large-scale recording and stimulating microdrive enables flexible brain network sampling
35 and modulation
36 - Minimally-perturbative causal network analysis reveals significant multiregional interactions
37 - Short-burst tetanic microstimulation suppresses neural excitability of multiregional
38 interactions
39 - Modulator's intrinsic activity predicts dynamics of neural excitability

SUMMARY

Electrical neuromodulation holds promise for treating neurological and neuropsychiatric disorders of the human brain, yet how neuromodulation alters processing within and between brain regions remains unclear. Here, we develop an implantable device to perform multisite, spatiotemporal, patterned microstimulation and recording across large-scale networks of the primate brain. We map a cortico-subcortical limbic network spanning the orbitofrontal cortex, anterior cingulate cortex, prefrontal cortex, the motor cortices, as well as the striatum, pallidum, and amygdala and test the network mechanism of action of short-burst tetanic microstimulation (SB-TetMS; ≤ 2 s, 100/200 Hz). By performing a minimally-perturbative causal network analysis, we dissociate network mechanisms of SB-TetMS-based neuromodulation. SB-TetMS acts to disrupt processing across projections that connect brain regions while leaving processing within regions relatively undisturbed. These results show that SB-TetMS provides a highly-effective procedure for modulating multiregional interactions and so has applications to treating a wide range of disorders of the human brain.

KEYWORDS

Multisite patterned microstimulation, causal network analysis, edge-modulation, node-modulation, intrinsic network dynamics

INTRODUCTION

Neuromodulation refers to a spectrum of technologies that seek to achieve therapeutic effects by intervening to alter neural activity. These technologies have broad and wide-ranging potential to treat refractory neurological and neuropsychiatric disorders (Johnson et al., 2013). Neuromodulation can be performed invasively with implantable devices as in deep brain stimulation (DBS) (Lozano et al., 2019) and direct cortical surface stimulation (Borchers et al., 2012). Neuromodulation can also be used to intervene non-invasively (Bikson et al., 2018; Fitzgerald et al., 2006; Folloni et al., 2019; Grossman et al., 2017; Legon et al., 2014; Tyler et al., 2018) and in the peripheral nervous system (Aaronson et al., 2017; Breit et al., 2018). Interventions with greater temporal or spatial precision are also under development in animal models (Chen et al., 2015, 2018; Gradinaru et al., 2009; Iaccarino et al., 2016; Martorell et al., 2019; Szablowski et al., 2018). Ultimately, neuromodulation-based technologies may be able to repair and even cure the disordered brain by recruiting neural plasticity (Braun et al., 2018; Johnson et al., 2013; Rajasethupathy et al., 2016).

Despite the therapeutic promise of neuromodulation, significant hurdles exist. While recent human studies show that electrical neuromodulation may enhance memory (Ezzyat et al., 2017, 2018; Inman et al., 2017; Suthana et al., 2012; Titiz et al., 2017), reduce impulsivity (Wu et al., 2017), and improve mood state (Rao et al., 2018) and cognitive control (Widge et al., 2019), whether and how electrical stimulation can be used to treat neuropsychiatric disorders remains controversial. Clinical studies report that electrical stimulation is not effective at treating early Alzheimer's (Leoutsakos et al., 2018) and treatment-resistant depression (Dougherty et al., 2015) and has negative effects, impairing spatial and verbal memory (Jacobs et al., 2016).

Clinical targets for therapeutic stimulation are increasingly viewed within a circuit-based model of neural dysfunction (Braun et al., 2018; McIntyre and Anderson, 2016; Williams, 2017).

Circuit-based models propose that dysfunction arises from interactions between neurons in different regions of the brain. Consistent with this, recent work shows that stimulation alters neuronal interactions by altering temporally-patterned network activity (de Hemptinne et al., 2015; Reinhart and Nguyen, 2019). The circuit-based model of neural dysfunction highlights the need to assess the network mechanism of action — how the intervention alters activity not just in one region but across many regions in a network. The circuit-based model also highlights the importance of connecting how neuromodulation affects single cells to understanding how it affects network function. In particular, the circuit-based view hypothesizes that neuromodulation specifically acts to modulate interactions between groups of neurons in networks.

Network neuroscience describes brain networks as being composed of nodes connected by edges to form graphs (Bassett et al., 2018). The edges can have different weights, reflecting different connection strengths. Network neuroscience thus provides a framework for testing circuit-model-based predictions. Neuromodulation may involve suppressing or strengthening the edge weight between two nodes — the edge-modulation hypothesis. Alternatively, neuromodulation may modulate the nodes themselves, suppressing or facilitating activity at those sites — the node-modulation hypothesis. The circuit-based model predicts that neuromodulation involves edge-modulation more than node-modulation. To test this prediction, we need to disambiguate edge-based processing from node-based processing. Edge weight is often estimated from correlations in activity of each node, summarized by the adjacency matrix (Bassett et al., 2018). However, correlation-based estimates of edge weight confound edge processing with node processing. This is because correlation-based estimates do not directly measure connection strength. The estimates are confounded by changes in activity at each node and common inputs to both nodes (Pesaran et al., 2018). As a result, the extent to which neuromodulation modulates edge-based and node-based processing remains unclear.

Here, we test the network mechanism of action of a neuromodulatory intervention, short-burst tetanic microstimulation (SB-TetMS; ≤ 2 s, 100/200 Hz), by stimulating and recording across the cortico-subcortical limbic network of two awake rhesus macaque monkeys, spanning orbitofrontal cortex (OFC), anterior cingulate cortex (ACC), prefrontal cortex (PFC), primary motor cortex (M1), striatum, globus pallidus (GP), and amygdala (Amyg). We use the concept of neural excitability, which describes how each node responds to input according to the weight of an edge, to causally estimate edge weight in a causal network analysis. The resulting causal network analysis permits a rigorous dissection of edge- and node-modulation hypotheses. **Figure 1**A illustrates the experimental design, which has three components. We first measure excitability by measuring the neural response across the network to a secondary intervention - an isolated single microstimulation pulse. We then deliver the primary intervention, a SB-TetMS TetMS pulse train, at sites in either gray matter or white matter. We then repeat the secondary intervention. Our results indicate that SB-TetMS, a high-frequency stimulation commonly used to treat a variety of brain disorders, overwhelmingly acts to disrupt processing across edges. Perhaps surprisingly, processing within nodes remains relatively undisturbed.

RESULTS

Targeting and Sampling the Cortico-Subcortical Limbic Network

To analyze neuromodulation across the cortical-subcortical limbic network, we developed a large-scale semi-chronic microdrive system (**Figures 1**B and **S1**A) (Dotson et al., 2017) to target and sample a large-scale brain network for causal network analysis (**Figures 1**B and **1**C). With this system, we targeted and repeatedly sampled a network spanning 15 cortical and subcortical brain regions. The sampled network included seven cortical regions: OFC combining medial OFC and lateral OFC, ACC, posterior cingulate cortex (PCC), PFC combining inferior, middle, and superior frontal gyri, M1, primary sensory cortex (S1), and posterior parietal cortex (PPC) combining superior parietal lobule (SPL), supramarginal gyrus (SMG), and precuneus (pCun); and eight subcortical regions: caudate nucleus (CN), putamen (Put), globus pallidus external (GPe), Amyg, presubiculum (PrS), substantia innominata (SI), basal forebrain nucleus (BFB), nucleus accumbens (NAc).

To target each brain region, we registered electrodes to anatomical magnetic resonance images (MRIs) and magnetic resonance angiograms (MRAs). To limit routes for infection, we customized the shape of the chamber and microdrive to each animal's anatomy and established that the chamber was sealed following implantation (**Figure 1**C). To limit damage when lowering electrodes, we only advanced a subset of electrodes along trajectories considered safe (**STAR Methods**). Finally, we co-registered the MRIs to the MNI Paxinos labels (Frey et al., 2011) to label each recording and stimulation site (**Figure S1**B). We successfully studied activity from 165 electrodes (50 tungsten and 115 Pt/Ir) in Monkey M for over 24 months and 208 Pt/Ir electrodes in Monkey A for over 12 months.

We tested long-term stability of neural recordings in two ways. First, we examined LFP activity during the movement epoch of a reaching task. **Figure 1**D-**1**F presents task-evoked LFP

activity for 67 depths along a sample electrode trajectory. Task-evoked LFP activity clearly increased and decreased in magnitude as the electrode transitioned into and out of gray matter, respectively. We also validated localization based on spiking. Increased task-evoked LFP activity was associated with increasing spiking activity (**Figure S1**). Patterns of spiking activity and task-evoked LFP activity were preserved over many months, demonstrating long-term stability of the implanted device.

The causal network analysis let us study neural interactions between sets of recording and stimulation sites located at nodes in the network. Across all 15 nodes, we sampled from a grand total of 4658 sites in Monkey M and 4897 sites in Monkey A (**Figure 1**G; **STAR Methods**). Across both monkeys, we obtained 15,734 non-overlapping samples from 21 cortico-cortical edges, 11,276 non-overlapping samples from 56 cortical-subcortical edges and 1087 non-overlapping samples from 28 subcortical-subcortical edges (**Figure 1**H; **STAR Methods**). We targeted our analysis to 9548 samples from the cortico-subcortical limbic network connecting OFC, ACC, PFC, CN, Put, and Amyg.

Causal Network Analysis Reveals Significant Directed Network Edges

We causally estimated edge weight with a secondary intervention delivering a single, low-amplitude, bipolar, biphasic, charge-balanced microstimulation pulse at a given node (Node1, the sender) while recording neural activity at other sampled network nodes (Node2, the receiver) (**Figure 2**A). Bipolar microstimulation limited the current spread from the stimulation site and corresponding stimulation artifacts. Bipolar re-referencing for recordings aimed to reveal focal evoked responses and also limited stimulation artifacts. The secondary intervention was designed to be minimally-perturbative (**Discussion**). By stimulating the sender above threshold and recording the receiver at threshold, the receiver response to input from the sender measured the weight of the network edge (sender→receiver). To do so, we stimulated the

178 sender with different current amplitude. We then set the stimulation dose at the threshold
179 needed to generate a stimulation-evoked response at receiver sites.
180
181 **Figure 2**A illustrates an example evoked LFP response in a CN site to single
182 microstimulation pulses (30 μA, 100 μs) delivered at an OFC site. Responses to isolated bipolar
183 microstimulation pulses appear to reflect responses by neurons in the receiver due to synaptic
184 inputs driven by stimulation at the sender. Consistent with this interpretation, single bipolar
185 microstimulation pulses were also able to drive spiking activity from neurons in the receiver,
186 peaking at the same time as the evoked LFP activity. This result indicates that bipolar re-
187 referenced LFP responses reflected a local neuronal source (**Figure 2**B). Averaging stimulation-
188 evoked responses across pulses revealed highly-significant evoked responses (**Figure 2**C).
189 Moreover, analyzing the spread of signals from the sender site to the receiver sites confirmed
190 that using bipolar microstimulation and recording configurations revealed focal responses and
191 could do so at the receiver sites distant to the sender (**Figure 2**C). We also performed control
192 recordings during monopolar microstimulation and confirmed that receiver site responses were
193 more likely to be contaminated by current spread (**Figure S2**).
194
195 To detect stimulation-evoked responses, we used an optimal signal detection algorithm
196 derived from an accumulating log-likelihood ratio (AccLLR) framework (Banerjee et al., 2010),
197 which we term stimAccLLR (**STAR Methods**). Across 12,721 pairs of sites tested in 132
198 network edges we causally sampled, we identified and characterized 78 significant functional
199 interactions in 21 network edges (**Figures 2**D and **2**E; **Table S1** and **S2**). On average, we
200 obtained a significant directed functional interaction between a pair of nodes with probability of
201 0.61% (**Discussion**). Since not all pairs of nodes are expected to functionally interact, we tested
202 whether some pairs of nodes interacted more than others (**Table S2**). A subset of the network
203 edges revealed significant directed functional interactions ($p < 0.05$, binomial test; **Figure 2**F

204 and **Figure S3**): OFC→CN (1.16%: 14/1212 samples, p = 0.009), OFC→PFC (1.16%: 9/779
205 samples, p = 0.027), OFC→M1 (6%: 6/100 samples, $p = 3.2\times10^{-5}$), CN→Put (4.46%: 5/112
206 samples, $p = 5.4\times10^{-4}$), and Amyg→OFC (10.17%: 6/59 samples, $p = 1.5\times10^{-6}$). We also
207 observed significant interactions within a single network node, such as CN→CN (1.23%: 7/568
208 samples, p = 0.035). Thus, the causal network analysis defined a cortical-subcortical limbic
209 network (OFC-PFC-M1-CN-Put-Amyg).
210
211 **SB-TetMS Suppresses Neural Excitability of Network Edges**
212 TetMS has been proposed to act as a neuromodulatory intervention with therapeutic potential
213 (Urdaneta et al., 2017). We asked whether the network mechanism of TetMS neuromodulation
214 is consistent with either or both of the edge- and node-modulation hypotheses. To do so, we
215 implemented an open-loop multisite spatiotemporal patterned microstimulation framework
216 combining SB-TetMS pulse train (100/200 Hz, 0.25-2 s, primary intervention) and isolated single
217 microstimulation pulses (secondary intervention). We used this framework to investigate how
218 TetMS at the primary intervention site, which we term a modulator, alters the neural excitability
219 of identified network edges and the node activity (**Figure 3**A).
220
221 We first tested the edge-modulation hypothesis. We asked whether the modulator alters
222 the connection strength of the directed network edge identified between the sender and receiver
223 (**Figure 3**A). We did so by first measuring the state of the directed functional interaction
224 between the sender and receiver before SB-TetMS using a Pre-tetanic stimulation-evoked
225 response. We then delivered the SB-TetMS at a modulator site that was not at the sender or the
226 receiver. Immediately after the SB-TetMS pulse train was delivered, we then repeated the
227 minimal perturbation with single microstimulation pulses at the sender to measure the Post-
228 tetanic receiver response. **Figure 3**B illustrates idealized potential outcomes for the edge-

229 modulation hypothesis by comparing the peak magnitude of the pulse-triggered evoked
230 response in both Pre-tetanic and Post-tetanic epochs.
231
232 We then tested whether SB-TetMS delivered at the modulator alters activity within the
233 receiver node alone, as predicted by the node-modulation hypothesis. We studied LFP activity
234 because it is clinically-important and yielded reliable, long-term recordings across the sampled
235 network. We quantified node activity using power in beta (β: 13-30 Hz) frequency band, a key
236 signature of node activity used in DBS studies (Little and Brown, 2014). We also quantified
237 power in high gamma (high-γ: 70-150 Hz) frequency band, a key signature of node activity that
238 reflects local spiking of populations of neurons (Manning et al., 2009; Pesaran et al., 2002; Rich
239 and Wallis, 2017). We quantified LFP power before the Pre-tetanic single pulse (Pre-state, 100
240 ms) and after the Post-tetanic single pulse (Post-state, 100 ms) (**Figure 3**A). Since the
241 response of the receiver to the Post-tetanic single pulse is due to the sender, we defined the
242 Post-state as activity shortly after the pulse-triggered evoked response (150-250 ms after the
243 Post-tetanic single pulse onset). **Figure 3**C illustrates the idealized potential outcomes of
244 suppression and facilitation for the receiver node-modulation hypothesis. We tested the 62
245 identified directed network edges in both Pre-tetanic and Post-tetanic epochs (up to 150 ms
246 after Pre/Post pulse onset). We measured the Post-tetanic evoked response shortly after the
247 end of the TetMS pulse train (median τ_{post}: 50 ms; **STAR Methods**).
248
249 **Figure 4**A-**4**D presents an example recording with a gray matter modulator. In this
250 example, we delivered single microstimulation pulses (40 μA, 100 μs/ph) at an Amyg sender.
251 We observed a significant pulse-triggered evoked response at an OFC receiver to the Pre-
252 tetanic single pulses (**Figure 4**B). The evoked response varied pulse-by-pulse (**Figure 4**C).
253 Importantly, the TetMS (30 μA, 100 μs/ph, 100 Hz, 50-500 ms) delivered at another OFC site
254 (**Figure 4**A) suppressed the OFC receiver response to the Post-tetanic single pulses (**Figure**

255 **4**B). Suppression was observable following each pulse (**Figure 4**C). Analyzing the Pre-state
256 RMS and Post-state RMS revealed that the OFC modulator slightly decreased the OFC receiver
257 β power after the TetMS (median RMS_{Pre} = 1.68 μV; median RMS_{Post} = 1.62 μV; p = 0.046,
258 Wilcoxon rank sum test; **Figure 4**D). In comparison, the TetMS did not significantly change the
259 high-γ power at the OFC receiver (p = 0.36; **Figure 4**D). Results for this Amyg-sender, OFC-
260 receiver, and OFC-modulator are consistent with both edge- and node-modulation mechanisms
261 of neuromodulation.
262
263 **Figure 4**E-**4**H presents an example with a white matter modulator. In this example, we
264 delivered single microstimulation pulses (30 μA, 100 μs/ph) at an OFC sender. We observed a
265 significant pulse-triggered evoked response at an ACC receiver (**Figure 4**F), which varied
266 pulse-by-pulse (**Figure 4**G). Following a TetMS (20 μA, 100 μs/ph, 200 Hz, 250 ms) delivered to
267 the corpus callosum (CC) (**Figure 4**E), we observed the ACC receiver responses was
268 suppressed (**Figure 4**F) pulse-by-pulse (**Figure 4**G). Analyzing the Pre-state and Post-state
269 power revealed that the CC modulator did not significantly change the ACC receiver β and high-
270 γ power, respectively, before and after the 250-ms TetMS (p = 0.31 and p = 0.48; **Figure 4**H).
271 This example of SB-TetMS at the white matter modulator reveals edge-modulation but not
272 node-modulation.
273
274 We performed SB-TetMS across eight modulators spanning a white matter and seven
275 gray matter sites (two cortical and five subcortical) (**Figure S3** and **Table S1**). SB-TetMS
276 suppressed all identified network edges except two that we could not measure due to
277 stimulation artifacts (60/62, **Table S1**). Receiver node-modulation was mixed. While gray matter
278 modulators significantly suppressed receiver node β power (11/40 nodes, $p = 2.55\times10^{-6}$,
279 binomial test), receiver node high-γ power did not significantly change (3/40 nodes, p = 0.19,
280 binomial test) and the white matter modulator did not significantly suppress either (β: 1/20

281 nodes, p = 0.38; high-γ: 3/20 nodes, p = 0.06, binomial test). These results demonstrate that
282 SB-TetMS exerts a widespread neuromodulatory influence and overwhelmingly acts to
283 suppress network edges, while receiver node-modulation is less consistent.
284
285 **Modulator Intrinsic Activity Predicts Dynamics of Neural Excitability of Network Edges**
286 The previous results demonstrate that SB-TetMS significantly modulates the receiver response
287 to the sender, the edge, but does not modulate the receiver node itself except when delivered in
288 the gray matter. A significant concern is that if SB-TetMS modulates the sender node, a change
289 in receiver node response may be incorrectly attributed to edge-modulation. This remains a
290 concern because we did not directly test sender node-modulation due to the presence of
291 stimulation artifacts at the sender following delivery of the isolated microstimulation pulse to the
292 sender. Therefore, to address this concern, we need a way to control for sender node-
293 modulation.
294
295 Edge-modulation varied pulse-by-pulse (**Figure 4**). We reasoned that pulse-by-pulse
296 edge-modulation may reflect an intrinsic network mechanism that modulates edge weight
297 between the sender and receiver nodes (**Figure 5**A). Activity at other network sites, which we
298 term modulators, may be associated with strengthening or weakening the edge weight pulse-by-
299 pulse. If so, edge-modulation may co-vary with modulator neural activity, allowing us to use
300 intrinsic network dynamics to control for the presence of sender node-modulation.
301
302 We first more closely examined moment-by-moment stimulation response dynamics.
303 **Figure 5**B-**5**D presents example activity from an Amyg→OFC network edge. We used
304 stimAccLLR procedure to detect response to each Pre-tetanic single pulse (**Figure S4**).
305 Impressively, along with 'Hit' events, we observed 'Miss' events when the receiver did not
306 respond to sender stimulation (**Figure 5**C). Consistent with the presence of two response

classes, multiunit activity was strongly driven in 'Hit' events, and not driven in 'Miss' events. (**Figure S5**). To test for the presence of two responses classes, we classified pulse-by-pulse evoked responses using a Gaussian mixture model (GMM). The GMM clustered pulse-evoked responses into two classes. For a majority of the identified directed network edge samples (50/78, 64%) the analysis methods agreed ($p < 0.05$, Fisher's exact test, two-tailed test; **Figure S6**). Thus, the results of the GMM and stimAccLLR provided convergent evidence for 'Hit' and 'Miss' stimulation response dynamics.

We then identified modulators by asking if we could predict 'Hit' and 'Miss' events from simultaneously recorded LFP activity at other sites in the sampled network during the baseline period before each Pre-tetanic single pulse (**STAR Methods**). Receiver operating characteristic (ROC) analysis detected 'Hit' events from 'Miss' events in frequency bands of theta (θ, 4-7 Hz; 794 sites), beta (β, 13-30 Hz; 758 sites), and gamma (γ, 32-60 Hz; 865 sites). **Figure 5**E present examples where the baseline β-power of a Put and PPC modulator co-varied with stimulation responses detected at the OFC receiver (**Figure 5**C). Reduced β-power of the Put modulator before the pulse onset significantly predicted missing responses recorded at the OFC receiver. In contrast, increased β-power of the PPC modulator significantly predicted missing responses. Across all modulators identified for a given network edge, we observed significant modulation of neural excitability. These results demonstrate that multiregional interactions are dynamically orchestrated by modulator activity distributed across the network.

With modulators in hand, we tested sender node-modulation hypothesis using sender node power immediately before each Pre-tetanic single pulse. If edge-modulation is explained by sender node-modulation, modulator activity should be correlated with the sender node activity. Our results show that modulator power did not correlate with sender node power in the θ, β, and γ frequency bands (θ: 604/794, 76%; β: 620/758, 82%; γ: 744/865, 86% not

333 significantly correlated sites, $p > 0.05$; **STAR Methods**). To confirm that this procedure provided
334 consistent results for receiver node-modulation, we asked whether the state of the receiver
335 before Pre-tetanic single pulse was also predicted by edge-modulation network activity. In
336 agreement with earlier analysis, modulator power did not significantly correlate with receiver
337 node power at most sites (θ: 435/794, 55%; β: 521/758, 69%; γ: 519/865, 60% not significantly
338 correlated sites, $p > 0.05$). Interestingly, receiver node activity was correlated with the modulator
339 activity more often than sender node activity ($p < 0.001$ for θ, β, and γ, Chi-squared test). These
340 results reinforce the conclusion that neuromodulation using SB-TetMS acts to modulate edges
341 more than either the sender node or the receiver node.

342 **DISCUSSION**

343 Our study performs a causal network analysis of the cortico-subcortical limbic network to identify
344 the network mechanism of action of SB-TetMS. By recording responses at receiver sites to the
345 delivery of isolated single microstimulation pulses at sender sites, we measured neural
346 excitability across several projections connecting OFC, ACC, PFC, motor cortex, CN, Put, and
347 Amyg. The causal network analysis reveals that neural excitability varies moment-by-moment.
348 Analyzing changes in neural excitability before and after SB-TetMS, we show that SB-TetMS
349 acts to disrupt processing across projections that connect brain regions, edges, while leaving
350 processing within regions, nodes, relatively undisturbed. Our results, obtained within a multisite
351 spatiotemporal patterned microstimulation framework, provide clear neurophysiological
352 evidence that SB-TetMS offers a highly-effective procedure for modulating multiregional
353 interactions, with important applications to treating disorders of large-scale brain networks.

354

355 **Minimally-Perturbative Causal Network Analysis**

356 Interactions across brain networks are often inferred from the structure of correlations in neural
357 activity and from examining responses to large-amplitude and/or trains of stimulation pulses.
358 However, interpreting specific activity patterns in a receiver as being due to interactions with a
359 sender is subject to several confounds. Correlations in activity between two nodes are also
360 sensitive to the confounding influence of common inputs from other brain regions. Consequently,
361 correlation-based sampling can yield network edges even when the receiver does not receive
362 any input from the sender (Pesaran et al., 2018). In contrast, while correlation-based sampling
363 can be used to infer the strength of directed functional interactions (Keller et al., 2011; Khambhati
364 et al., 2019; Solomon et al., 2018), causal sampling offers a more direct measure of functional
365 interactions.

366

367 Inferring directed functional interactions by delivering either large-amplitude stimulation
368 pulse or multiple stimulation pulses in pulse trains suffers other confounds. Since stimulation
369 changes neural activity, stimulating may recruit network responses due to other mechanisms
370 (Herrington et al., 2016). If so, the measurement changes the interaction instead of probing the
371 interaction. Delivering a single low-amplitude (10-100 μA) microstimulation pulse therefore offers
372 the opportunity to probe network state while avoiding the confounding effects and network
373 responses elicited by macrostimulation pulses and pulse trains.
374
375 Our results provide multiple lines of evidence that the impact of the secondary
376 intervention is minimally-perturbative. First, we used single, bipolar, biphasic pulses of relatively
377 low-amplitude that are not necessarily expected to generate large-scale network responses.
378 Indeed, single microstimulation pulse has not been previously used to map large-scale networks
379 in the awake primate brain. The natural concern is that network responses following such
380 minimal perturbations may not be detectable. Second, following single microstimulation pulses
381 we observed sparse directed functional interactions instead of widespread network effects.
382 Approximately 0.6% of sampled sites showed statistically-significant responses. We should note
383 that sparsity may result from the presence of residual stimulation artifacts that obscure
384 responses at some sites. The degree of sparsity likely also reflects the minimally-perturbative
385 microstimulation approach we used, which is conservative and so may fail to drive detectable
386 responses at some sites where more pre-synaptic inputs might be required to produce
387 excitatory post-synaptic activity (Häusser et al., 2001). Sparsity also likely reflects the underlying
388 anatomical connections and the fact that many recording sites may not receive inputs from the
389 sender. Third, although the responses were sparse, they were strong, visible on a single-pulse
390 basis, and varied moment-by-moment. The presence of strong pulse-evoked responses
391 demonstrates the efficacy of the intervention and mitigates concern about false positives due to
392 multiple comparisons involving the number of tested network edges. The absence of pulse-

evoked responses at other times also demonstrates the receiver is perturbed at threshold and hence that the secondary intervention is unlikely to be altering interactions across the network.

Network Mechanisms of Action of SB-TetMS

A large body of work has shown that electrical stimulation preferentially activates axons not somas, which could cause both orthodromic and antidromic stimulation effects (Aberra et al., 2018; Histed et al., 2009; Rattay, 1999; Tehovnik and Slocum, 2013; Tehovnik et al., 2006). Antidromic responses tend to be stereotyped while orthodromic responses are more variable, especially if trans-synaptically mediated (Klink et al., 2017; Tehovnik and Slocum, 2013; Tolias et al., 2005). The variable response to single pulses we observed therefore suggests they are mediated orthodromically and trans-synaptically. The pulse-evoked LFP activity modulated by SB-TetMS depends on the excitatory (e.g. AMPA) and inhibitory (e.g. GABA)-mediated post-synaptic potentials at the receiver and their spatial distribution in response to pre-synaptic inputs from the sender. Changes due to SB-TetMS may, therefore, change the relative strength of excitatory and inhibitory responses, reducing excitatory and increasing inhibitory potentials. This would be consistent with reductions in firing rate we observed. Alternatively, SB-TetMS mediated changes may also induce spatial reorganization of the pre-synaptic inputs that changes the strength of effective dipole moment generating the observed LFP activity (Mazzoni et al., 2015). SB-TetMS mediated changes in pre-synaptic inputs may also disrupt excitatory-inhibitory balance to induce long-term synaptic plasticity (Froemke, 2015). The absence of responses following SB-TetMS that we observed might also reflect short-term depression in the post-synaptic neurons.

Since network edges in multiregional networks reflect anatomical projection systems containing white matter fiber tracts (Bassett and Sporns, 2017), the modulation of edges we observed likely reflects axonal effects. This suggests that SB-TetMS delivered to the white

matter should have the greatest impact on multiregional interactions. However, we found that SB-TetMS in white matter did not modulate receiver node activity overall even when receiver node responses to stimulation of the sender were suppressed. Instead, our findings reinforce a body of work showing that high-frequency stimulation at white matter modulator sites can disrupt or block synaptic transmission from the sender to receiver (Grill et al., 2004; Jensen and Durand, 2009; Lozano et al., 2019). Such effects are said to induce 'information lesions', highlighting the potential for SB-TetMS as a tool to dynamically reconfigure network information processing.

Interestingly, SB-TetMS delivered to the gray matter not only suppressed the edge weight (100% of sites tested) but also reduced the β-activity at a significant minority of receiver nodes (27.5%). Beta-band suppression by gray matter SB-TetMS is consistent with an alternative 'synaptic filtering' hypothesis. According to synaptic filtering, a high-frequency stimulation pulse train delivered to the pre-synaptic site induces short-term suppression that selectively suppresses the synaptic transmission of low-frequency content contained in stimulation-induced neural activity at the post-synaptic site (Rosenbaum et al., 2014). This potential mechanism merits further investigation to examine changes on a longer time scale, and may involve stimulation-induced long-term synaptic plasticity changes mediated by the interplay between neuronal and non-neuronal cells, like astrocytes (McIntyre and Anderson, 2016). Examining changes due to long-term plasticity will be especially important for assessing how other neural pathways compensate for disruptions to maladaptive networks and dynamically reconfigure network functions (Johnson et al., 2013).

Two recent studies have used isolated pulses as a secondary intervention and a pulse train as a primary intervention to examine changes in neural excitability across brain networks (Keller et al., 2018; Rao et al., 2018). Unlike our approach, both studies applied primary and

445 secondary interventions at the same site. As a result, node-based and edge-based mechanisms
446 could not be dissociated specifically limiting the strength of conclusions regarding the network
447 mechanism of action. When both primary and secondary interventions are delivered to the
448 sender, any changes in the response of the receiver could have at least two origins. Changes in
449 the receiver node response may reflect changes in pre-synaptic activity recruited by the
450 secondary intervention. Changes in the receiver response may also reflect changes in the
451 impact of the primary intervention on the sender (Siebner et al., 2004). By delivering the primary
452 and secondary interventions to different sites, we could disambiguate the effects and investigate
453 dynamic changes in the weight of identified edges connecting different senders and receivers.
454 Critically, we could do so independently of intrinsic node activity at both the sender and the
455 receiver to specifically conclude that edge-based responses were disrupted.
456
457 We should also note that suppression of the evoked response to the Post-tetanic single
458 pulse may be confounded by an effect related to the phase of inhibition after the excitatory
459 response to the Pre-tetanic single pulse (Butovas and Schwarz, 2006; Logothetis et al., 2010;
460 Seidemann et al., 2002) or related to suppressed responses to paired microstimulation pulses
461 (Butovas and Schwarz, 2006; Castro-Alamancos and Connors, 1996). Our experimental design
462 employed Pre-tetanic and Post-tetanic single pulses separated by 0.75-3 s, mitigating such
463 concerns.
464
465 **Intrinsic Network Dynamics Reveal Modulation Networks**
466 The effects of SB-TetMS we report extend beyond putatively direct interactions. Our results
467 uncover hints of network mechanisms of neuromodulation. When examined pulse-by-pulse, the
468 causal network analysis revealed dynamics in the stimulation responses, suggesting that
469 changes in neural excitability can generate a form of network gating. By analyzing intrinsic
470 network dynamics before Pre-tetanic single pulses, we revealed sets of sites with activity that

471 can predict the changes in neural excitability between the sender and receiver. The presence of
472 these modulator sites showed that neuromodulation of neural excitability did not significantly
473 correlate with activity of both sender and receiver and was more likely to display receiver node-
474 modulation than sender node-modulation. Our experiments, however, did not constrain the
475 mechanism by which the modulator sites modulate neural excitability. We were not able to, for
476 example, test whether single-pulse stimulation of modulator sites drove responses in the
477 associated receiver nodes. Therefore, how modulators interact with the receiver and can
478 specifically modulate pre-synaptic inputs from the sender remains open.
479

480 **Implications for Personalized Neuromodulation for Neuropsychiatric Disorders**

481 The cortico-subcortical limbic network that we investigated plays a central role in mood
482 regulation (Drevets, 2001; Drysdale et al., 2017; Price and Drevets, 2010; Sani et al., 2018) and
483 reward processing (Nestler and Carlezon, 2006). Dysfunctions of this network, which disrupt the
484 learning of stimulus-reward encoding map in decision-making and motivation, underlie many
485 neuropsychiatric conditions. The clinical heterogeneity of these conditions affects multiple
486 overlapping circuits (Drysdale et al., 2017). How to identify appropriate biomarkers to correct
487 maladaptive neural circuits for effective treatment still remains challenging (Johnson et al.,
488 2013; Lozano et al., 2019). For example, several brain regions have been tested as stimulation
489 targets to treat depression, including subgenual cingulate cortex (Mayberg et al., 2005), lateral
490 OFC for (Rao et al., 2018), Amyg (Inman et al., 2018), and ventral capsule/ventral striatum
491 (Dougherty et al., 2015; Widge et al., 2019). However, the efficacy of stimulation has been
492 inconsistent across subjects. Inter-subject variability highlights the need to better understand
493 how to leverage intrinsic neural dynamics and neural plasticity across subjects in order to
494 restore normal stimulus-reward associations.
495

496 Our results offer new insights into how SB-TetMS may act to preferentially disrupt
497 processing across projections. For example, if we can identify damaged projection systems as
498 biomarkers of specific clinical-symptom profiles (Drysdale et al., 2017), applying SB-TetMS to
499 the identified projection systems may unwire the pathological connections and reconfigure
500 functional connectivity to normal state. Over the course of SB-TetMS treatment, a minimally-
501 perturbative casual network analysis can also assess and track how maladaptive multiregional
502 interactions are reconfigured in response to the treatment. Personalized, subject-specific
503 adjustments in how SB-TetMS is targeted as networks reconfigure may improve treatment
504 efficacy.
505
506 Going beyond focal electrical stimulation to target specific brain regions, our findings
507 imply that modulators distributed across interconnected networks may be effective targets for
508 SB-TetMS to modulate dynamics of multiregional interactions. Future work will likely benefit
509 from the ability to predict dynamic reconfiguration of modulation networks by optimizing
510 temporal and spatial patterns of stimulation (Choi et al., 2016; Khambhati et al., 2019; Muldoon
511 et al., 2016). To improve the precision of targeting multiregional projection systems, diffusion
512 tractography may be useful for developing a rational and personalized approach to probing
513 network dynamics (Riva-Posse et al., 2017). Guided by tractography, we can define each
514 individual's list of stimulation sites and compare possible differences in the impact of stimulation.
515 Conversely, when a stimulation site is discovered, we can identify projection systems to support
516 more detailed causal network perturbations. Finally, our approach using minimally-perturbative
517 causal network analysis can be generalized to uncover network mechanisms of action for other
518 neuromodulation modalities.

519 **Figure Legends**

520 **Figure 1. Large-scale Semi-chronic Microdrive System Enables Targeting and Repeated**
521 **Sampling of the Cortico-Subcortical Limbic Network**

522 (A) Experimental design using multisite spatiotemporal patterned microstimulation framework to
523 test alternative neuromodulation hypotheses of network mechanisms of action of SB-TetMS-
524 based intervention (primary) — edge-modulation versus node-modulation.

525 (B) A solid model of the customized semi-chronic large-scale microdrive assembly.

526 (C) Implanted microdrive chamber co-registered with the MRI-based skull and brain surface
527 reconstruction. Vertical black lines represent the co-registered electrodes in a given recording
528 session. Anterior (A), posterior (P), dorsal (D), and ventral (V) directions are indicated.

529 (D) White and gray matter transitions of averaged evoked LFP patterns recorded from an
530 example electrode in reaching epoch as the electrode travels through corpus callosum (CC),
531 caudate nucleus (CN), internal capsule (IC), and external globus pallidus (GPe). Electrode
532 depth was estimated from the cortical surface.

533 (E) Co-registered four samples of the electrode depth in CC, CN, IC, and GPe on the coronal
534 MRI slice. Dorsal (D), ventral (V), left (L), and right (R) directions are indicated.

535 (F) Co-registration of the electrode tracks with anatomical parcellation of frontal lobe of Monkey
536 M. Black dots represent the overlaid electrode grid. Yellow dot is the example electrode at the
537 horizontal MRI slice depth in CN. Anterior (A), posterior (P), lateral (L), and medial (M)
538 directions are indicated.

539 (G) Sampled brain regions (network nodes) illustrated using a DTI-based MR rhesus macaque
540 brain atlas (Calabrese et al., 2015) from the Scalable Brain Atlas. Anterior (A), posterior (P),
541 dorsal (D), ventral (V), left (L), and right (R) directions are indicated.

542 (H) Non-overlapping network edge samples between sampled network nodes. Anterior (A),
543 posterior (P), dorsal (D), and ventral (V) directions are indicated.

544 See also **Figure S1**.

545 **Figure 2. Causal Network Analysis Identifies Directed Network Edges**

546 (A) Using single, bipolar, biphasic, charge-balanced microstimulation pulses at the sender to
547 causally sample network edge that showed directed functional interaction between the sender
548 and receiver (sender→receiver). Example of a pulse event recorded at a CN receiver in
549 response to a single microstimulation pulse delivered at an OFC sender (30 μA, 100 μs/ph). We
550 defined the epoch before pulse onset as "Pulse Null" and the epoch after pulse onset as "Pulse
551 Event".

552 (B) Example showing single bipolar microstimulation pulses (10 μA, 100 μs/ph) at an OFC
553 sender drove both multiunit activity and LFP response recorded at a CN receiver, peaking
554 approximately at 46 ms after the pulse onset. Data from -1 ms to 5 ms around the pulse onset
555 were not used for multiunit activity analysis due to stimulation artifact. Error values of evoked
556 LFP response are s.e.m. (n = 52). Anterior (A), posterior (P), lateral (L), and medial (M)
557 directions are indicated.

558 (C) Example showing delivery of single bipolar microstimulation pulses (50 μA, 100 μs/ph) at an
559 OFC sender revealed the significant focal evoked LFP responses recorded at two sites in the
560 principal sulcus (ps) distant from the stimulating site, rather than at the site nearby. MRI on the
561 left is overlaid at the depth of the OFC stimulating sites (magenta dots). MRI on the right is
562 overlaid at the depth of the ps recording sites (blue dots). Anterior (A), posterior (P), lateral (L),
563 and medial (M) directions are indicated.

564 (D) Scatter plots of average response latencies and correct detection rates of detected network
565 edge samples that showed directed functional interactions (Monkey M, 40; Monkey A, 38).

566 (E) Histograms of the average response latencies and correct detection rates of all detected
567 network edge samples.

568 (F) Diagram of the network edges showing statistically significant directed functional
569 interactions. Anterior (A), posterior (P), dorsal (D), and ventral (V) directions are indicated.

570 See also **Figures S2** and **S3**, **Tables S1** and **S2**.

571 **Figure 3. Conceptual Framework to Test Edge-Modulation and Receiver Node-Modulation**
572 **Hypotheses**

573 (A) Design of the multisite spatiotemporal patterned microstimulation framework to test network
574 mechanisms of SB-TetMS — edge-modulation versus receiver node-modulation hypotheses.
575 Illustration of how a SB-TetMS delivered at a modulator site affects the edge weight and the
576 receiver node activity. For each stimulation bout, τ_{Pre} is the post Pre-tetanic single pulse epoch
577 before the TetMS onset, T is the duration of TetMS with a given frequency (f_{stim}), and τ_{Post} is the
578 latency between TetMS offset and Post-tetanic single pulse onset. The gray shaded rectangles
579 are the 100-ms epochs for computing Pre-state RMS and Post-state RMS of the neural activity
580 recorded at the receiver, respectively.

581 (B) Illustration of testing edge-modulation hypothesis by comparing Pre-tetanic and Post-tetanic
582 evoked potentials.

583 (C) Illustration of testing receiver node-modulation hypothesis by comparing the RMS of neural
584 Pre-state and Post-state activity recorded at the receiver. RMS denotes the root mean square.

585 **Figure 4. SB-TetMS Suppresses Directed Functional Interactions across Network Edges**

586 (A) Example of how a SB-TetMS (T = 50-500 ms, f_{stim} = 100 Hz, 30 μA, 100 μs/ph) delivered at
587 an OFC modulator (orange dots) suppressed the directed functional interaction across a
588 network edge Amyg→OFC revealed by evoked response in OFC (blue dot) to single
589 microstimulation pulses (40 μA, 100 μs/ph; τ_{Pre} = 500 ms and τ_{Post} = 25-100 ms) delivered at an
590 OFC sender (magenta dots). Anterior (A), posterior (P), lateral (L), and medial (M) directions are
591 indicated.

592 (B) Z-scored pulse-triggered average LFP responses (n = 322) to Pre-tetanic and Post-tetanic
593 single pulses for the example network edge Amyg→OFC, respectively.

594 (C) Heat map of evoked LFP responses recorded at the OFC receiver across all events during
595 Pre-tetanic and Post-tetanic epochs, respectively.

596 (D) Scatter plots of Pre-state RMS versus Post-state RMS of β and high-γ neural activity of the
597 OFC receiver, respectively. p = 0.046 (β) and 0.36 (high-γ), Wilcoxon rank sum test. RMS
598 denotes the root mean square.

599 (E) Example of how a SB-TetMS (T = 250 ms, f_{stim} = 200 Hz, 20 μA, 100 μs/ph) delivered at a
600 modulator in corpus callosum (CC, orange dots) suppressed the directed functional interaction
601 across a network edge OFC→ACC revealed by evoked response in ACC (blue dot) to single
602 microstimulation pulses (30 μA, 100 μs/ph; τ_{Pre} = 500 ms and τ_{Post} = 0, 50 ms) delivered in OFC
603 (magenta dots). as: arcuate sulcus; cs: central sulcus; ps: principal sulcus; Anterior (A),
604 posterior (P), lateral (L), and medial (M) directions are indicated.

605 (F) Z-scored pulse-triggered average LFP responses (n = 110) to Pre-tetanic and Post-tetanic
606 single pulses for the example network edge OFC→ACC, respectively.

607 (G) Heat map of the evoked LFP responses recorded at the ACC receiver across all events
608 during Pre- and Post-tetanic epochs, respectively.

609 (H) Scatter plots of Pre-state RMS versus Post-state RMS of β and high-γ neural activity of the
610 ACC receiver, respectively. p = 0.31 (β) and 0.48 (high-γ), Wilcoxon rank sum test.

611 **Figure 5. Intrinsic Network Activity Predicts Dynamics of Neural Excitability**

612 (A) Illustration of dynamics of directed functional interaction from the sender to receiver
613 modulated by intrinsic network dynamics of modulators.

614 (B) Illustration of directed functional interaction across the example network edge Amyg→OFC
615 (**Figure 4**A) modulated by the intrinsic activity recorded at a Put and PPC modulator (as:
616 arcuate sulcus; ips: intraparietal sulcus). Anterior (A), posterior (P), dorsal (D), ventral (V),
617 lateral (L), and medial (M) directions are indicated.

618 (C) Heat map of the evoked LFP responses recorded at the OFC receiver. Waveforms are
619 sorted by latency marked as black crosses. First 5-ms data after the pulse onset were not used
620 due to stimulation artifact. The best correct detect performance decoding single microstimulation
621 pulse of LFP response was 64%, with a 30% false alarm and 6% unknown. The average
622 response latency at this false alarm rate was 64 ms.

623 (D) Pulse-triggered average evoked responses for correctly detected 'Hit' events (black, n =
624 206) and not detected 'Miss' events (green, n = 116). Error values are s.e.m.

625 (E) Spectrograms of the baseline LFP activity (before Pre-tetanic single pulse onset) of a Put
626 and PPC modulator, respectively, computed as z-score magnitude of difference between 'Hit'
627 and 'Miss' events detected based on the stimulation responses recorded at the OFC receiver.
628 Black contour highlights the area of significance (permutation test, cluster-corrected for multiple
629 comparisons; n = 10,000, $p < 0.05$, two-tailed test).

630 **References**

631 Aaronson, S.T., Sears, P., Ruvuna, F., Bunker, M., Conway, C.R., Dougherty, D.D., Reimherr,
632 F.W., Schwartz, T.L., and Zajecka, J.M. (2017). A 5-year observational study of patients with
633 treatment-resistant depression treated with vagus nerve stimulation or treatment as ssual:
634 comparison of response, remission, and suicidality. Am. J. Psychiatry *174*, 640–648.

635 Aberra, A.S., Peterchev, A. V, and Grill, W.M. (2018). Biophysically realistic neuron models for
636 simulation of cortical stimulation. J. Neural Eng. *15*, 066023.

637 Andersson, J.L.R., and Sotiropoulos, S.N. (2015). Non-parametric representation and prediction
638 of single- and multi-shell diffusion-weighted MRI data using Gaussian processes. Neuroimage
639 *122*, 166–176.

640 Banerjee, A., Dean, H.L., and Pesaran, B. (2010). A likelihood method for computing selection
641 times in spiking and local field potential activity. J. Neurophysiol. *104*, 3705–3720.

642 Bassett, D.S., and Sporns, O. (2017). Network neuroscience. Nat. Neurosci. *20*, 353–364.

643 Bassett, D.S., Zurn, P., and Gold, J.I. (2018). On the nature and use of models in network
644 neuroscience. Nat. Rev. Neurosci. *19*, 566–578.

645 Bikson, M., Brunoni, A.R., Charvet, L.E., Clark, V.P., Cohen, L.G., Deng, Z. De, Dmochowski,
646 J., Edwards, D.J., Frohlich, F., Kappenman, E.S., et al. (2018). Rigor and reproducibility in
647 research with transcranial electrical stimulation: An NIMH-sponsored workshop. Brain Stimul.
648 *11*, 465–480.

649 Borchers, S., Himmelbach, M., Logothetis, N., and Karnath, H.-O. (2012). Direct electrical
650 stimulation of human cortex — the gold standard for mapping brain functions? Nat. Rev.
651 Neurosci. *13*, 63–70.

652 Braun, U., Schaefer, A., Betzel, R.F., Tost, H., Meyer-Lindenberg, A., and Bassett, D.S. (2018).
653 From maps to multi-dimensional network mechanisms of mental disorders. Neuron *97*, 14–31.

654 Breit, S., Kupferberg, A., Rogler, G., and Hasler, G. (2018). Vagus nerve as modulator of the
655 brain-gut axis in psychiatric and inflammatory disorders. Front. Psychiatry *9*, 1.

656 Butovas, S., and Schwarz, C. (2006). Spatiotemporal effects of microstimulation in rat
657 neocortex: a parametric study using multielectrode recordings. J. Neurophysiol. *90*, 3024–3039.

658 Calabrese, E., Badea, A., Coe, C.L., Lubach, G.R., Shi, Y., Styner, M.A., and Johnson, G.A.
659 (2015). A diffusion tensor MRI atlas of the postmortem rhesus macaque brain. Neuroimage *117*,
660 408–416.

661 Castro-Alamancos, M., and Connors, B. (1996). Spatiotemporal properties of short-term
662 plasticity sensorimotor thalamocortical pathways of the rat. J. Neurosci. *16*, 2767–2779.

663 Chen, R., Romero, G., Christiansen, M.G., Mohr, A., and Anikeeva, P. (2015). Wireless
664 magnetothermal deep brain stimulation. Science *347*, 1477–1480.

665 Chen, S., Weitemier, A.Z., Zeng, X., He, L., Wang, X., Tao, Y., Huang, A.J.Y., Hashimotodani,
666 Y., Kano, M., Iwasaki, H., et al. (2018). Near-infrared deep brain stimulation via upconversion
667 nanoparticle-mediated optogenetics. Science *359*, 679–684.

668 Choi, J.S., Brockmeier, A.J., McNiel, D.B., Kraus, L.M. von, Príncipe, J.C., and Francis, J.T.
669 (2016). Eliciting naturalistic cortical responses with a sensory prosthesis via optimized
670 microstimulation. J. Neural Eng. *13*, 056007.

671 Dotson, N.M., Hoffman, S.J., Goodell, B., and Gray, C.M. (2017). A large-scale semi-chronic

672 microdrive recording system for non-human primates. Neuron *96*, 769-782.e2.

673 Dougherty, D.D., Rezai, A.R., Carpenter, L.L., Howland, R.H., Bhati, M.T., O'Reardon, J.P.,
674 Eskandar, E.N., Baltuch, G.H., Machado, A.D., Kondziolka, D., et al. (2015). A randomized
675 sham-controlled trial of deep brain stimulation of the ventral capsule/ventral striatum for chronic
676 treatment-resistant depression. Biol. Psychiatry *78*, 240–248.

677 Drevets, W.C. (2001). Neuroimaging and neuropathological studies of depression: implications
678 for the cognitive-emotional features of mood disorders. Curr. Opin. Neurobiol. *11*, 240–249.

679 Drysdale, A.T., Grosenick, L., Downar, J., Dunlop, K., Mansouri, F., Meng, Y., Fetcho, R.N.,
680 Zebley, B., Oathes, D.J., Etkin, A., et al. (2017). Resting-state connectivity biomarkers define
681 neurophysiological subtypes of depression. Nat. Med. *23*, 28–38.

682 Ezzyat, Y., Kragel, J.E., Burke, J.F., Levy, D.F., Lyalenko, A., Wanda, P., O'Sullivan, L., Hurley,
683 K.B., Busygin, S., Pedisich, I., et al. (2017). Direct brain stimulation modulates encoding states
684 and memory performance in humans. Curr. Biol. *27*, 1251–1258.

685 Ezzyat, Y., Wanda, P.A., Levy, D.F., Kadel, A., Aka, A., Pedisich, I., Sperling, M.R., Sharan,
686 A.D., Lega, B.C., Burks, A., et al. (2018). Closed-loop stimulation of temporal cortex rescues
687 functional networks and improves memory. Nat. Commun. *9*, 365.

688 Fitzgerald, P.B., Fountain, S., and Daskalakis, Z.J. (2006). A comprehensive review of the
689 effects of rTMS on motor cortical excitability and inhibition. Clin. Neurophysiol. *117*, 2584–2596.

690 Folloni, D., Verhagen, L., Mars, R.B., Fouragnan, E., Constans, C., Aubry, J.-F., Rushworth,
691 M.F.S., and Sallet, J. (2019). Manipulation of subcortical and deep cortical activity in the primate
692 brain using transcranial focused ultrasound stimulation. Neuron.

693 Frey, S., Pandya, D.N., Chakravarty, M.M., Bailey, L., Petrides, M., and Collins, D.L. (2011). An
694 MRI based average macaque monkey stereotaxic atlas and space (MNI monkey space).
695 Neuroimage *55*, 1435–1442.

696 Froemke, R.C. (2015). Plasticity of cortical excitatory-inhibitory balance. Annu. Rev. Neurosci.
697 *38*, 195–219.

698 Gradinaru, V., Mogri, M., Thompson, K.R., Henderson, J.M., and Deisseroth, K. (2009). Optical
699 deconstruction of parkinsonian neural circuitry. Science (80-.). *324*, 354–359.

700 Grill, W.M., Snyder, A.N., and Miocinovic, S. (2004). Deep brain stimulation creates an
701 informational lesion of the stimulated nucleus. Neuroreport *15*, 1137–1140.

702 Grossman, N., Bono, D., Dedic, N., Kodandaramaiah, S.B., Rudenko, A., Suk, H.J., Cassara,
703 A.M., Neufeld, E., Kuster, N., Tsai, L.H., et al. (2017). Noninvasive deep brain stimulation via
704 temporally interfering electric fields. Cell *169*, 1029-1041.e16.

705 Häusser, M., Major, G., and Stuart, G.J. (2001). Differential shunting of EPSPs by action
706 potentials. Science *291*, 138–141.

707 de Hemptinne, C., Swann, N.C., Ostrem, J.L., Ryapolova-Webb, E.S., San Luciano, M.,
708 Galifianakis, N.B., and Starr, P.A. (2015). Therapeutic deep brain stimulation reduces cortical
709 phase-amplitude coupling in Parkinson's disease. Nat. Neurosci. *18*, 779–786.

710 Herrington, T.M., Cheng, J.J., and Eskandar, E.N. (2016). Mechanisms of deep brain
711 stimulation. J. Neurophysiol. *115*, 19–38.

712 Histed, M.H., Bonin, V., and Reid, R.C. (2009). Direct activation of sparse, distributed
713 populations of cortical neurons by electrical microstimulation. Neuron *63*, 508–522.

714 Iaccarino, H.F., Singer, A.C., Martorell, A.J., Rudenko, A., Gao, F., Gillingham, T.Z., Mathys, H.,

715 Seo, J., Kritskiy, O., Abdurrob, F., et al. (2016). Gamma frequency entrainment attenuates
716 amyloid load and modifies microglia. Nature *540*, 230–235.

717 Inman, C.S., Manns, J.R., Bijanki, K.R., Bass, D.I., Hamann, S., Drane, D.L., Fasano, R.E.,
718 Kovach, C.K., Gross, R.E., and Willie, J.T. (2017). Direct electrical stimulation of the amygdala
719 enhances declarative memory in humans. Proc. Natl. Acad. Sci. U. S. A. 201714058.

720 Inman, C.S., Bijanki, K.R., Bass, D.I., Gross, R.E., Hamann, S., and Willie, J.T. (2018). Human
721 amygdala stimulation effects on emotion physiology and emotional experience.
722 Neuropsychologia.

723 Jacobs, J., Miller, J., Lee, S.A., Coffey, T., Watrous, A.J., Sperling, M.R., Sharan, A., Worrell,
724 G., Berry, B., Lega, B., et al. (2016). Direct Electrical Stimulation of the Human Entorhinal
725 Region and Hippocampus Impairs Memory. Neuron *92*, 983–990.

726 Jbabdi, S., Sotiropoulos, S.N., Savio, A.M., Graña, M., and Behrens, T.E.J. (2012). Model-
727 based analysis of multishell diffusion MR data for tractography: How to get over fitting problems.
728 Magn. Reson. Med. *68*, 1846–1855.

729 Jensen, A.L., and Durand, D.M. (2009). High frequency stimulation can block axonal
730 conduction. Exp. Neurol. *220*, 57–70.

731 Johnson, M.D., Lim, H.H., Netoff, T.I., Connolly, A.T., Johnson, N., Roy, A., Holt, A., Lim, K.O.,
732 Carey, J.R., Vitek, J.L., et al. (2013). Neuromodulation for brain disorders: challenges and
733 opportunities. IEEE Trans Biomed Eng *60*, 610–624.

734 Keller, C.J., Bickel, S., Entz, L., Ulbert, I., Milham, M.P., Kelly, C., and Mehta, A.D. (2011).
735 Intrinsic functional architecture predicts electrically evoked responses in the human brain. Proc.
736 Natl. Acad. Sci. U. S. A. *108*, 10308–10313.

737 Keller, C.J., Huang, Y., Herrero, J.L., Fini, M.E., Du, V., Lado, F.A., Honey, C.J., and Mehta,
738 A.D. (2018). Induction and quantification of excitability changes in human cortical networks. J.
739 Neurosci. *38*, 5384–5398.

740 Khambhati, A.N., Kahn, A.E., Costantini, J., Ezzyat, Y., Solomon, E.A., Gross, R.E., Jobst, B.C.,
741 Sheth, S.A., Zaghloul, K.A., Worrell, G., et al. (2019). Functional control of electrophysiological
742 network architecture using direct neurostimulation in humans. Netw. Neurosci. 1–30.

743 Klink, P.C., Dagnino, B., Gariel-Mathis, M.A., and Roelfsema, P.R. (2017). Distinct feedforward
744 and feedback effects of microstimulation in visual cortex reveal neural mechanisms of texture
745 segregation. Neuron *95*, 209-220.e3.

746 Legon, W., Sato, T.F., Opitz, A., Mueller, J., Barbour, A., Williams, A., and Tyler, W.J. (2014).
747 Transcranial focused ultrasound modulates the activity of primary somatosensory cortex in
748 humans. Nat. Neurosci. *17*, 322–329.

749 Leoutsakos, J.-M.S., Yan, H., Anderson, W.S., Asaad, W.F., Baltuch, G., Burke, A.,
750 Chakravarty, M.M., Drake, K.E., Foote, K.D., Fosdick, L., et al. (2018). Deep brain stimulation
751 targeting the fornix for mild Alzheimer dementia (the ADvance Trial): a two year follow-up
752 including results of delayed activation. J. Alzheimer's Dis. *64*, 597–606.

753 Little, S., and Brown, P. (2014). The functional role of beta oscillations in Parkinson's disease.
754 Parkinsonism Relat. Disord. *20*, S44–S48.

755 Logothetis, N.K., Augath, M., Murayama, Y., Rauch, A., Sultan, F., Goense, J., Oeltermann, A.,
756 and Merkle, H. (2010). The effects of electrical microstimulation on cortical signal propagation.
757 Nat. Neurosci. *13*, 1283–1291.

758 Lozano, A.M., Lipsman, N., Bergman, H., Brown, P., Chabardes, S., Chang, J.W., Matthews, K.,

759 McIntyre, C.C., Schlaepfer, T.E., Schulder, M., et al. (2019). Deep brain stimulation: current
760 challenges and future directions. Nat. Rev. Neurol. *15*, 148–160.

761 Manning, J.R., Jacobs, J., Fried, I., and Kahana, M.J. (2009). Broadband shifts in local field
762 potential power spectra are correlated with single-neuron spiking in humans. J. Neurosci. *29*,
763 13613–13620.

764 Maris, E., Schoffelen, J.-M., and Fries, P. (2007). Nonparametric statistical testing of coherence
765 differences. J. Neurosci. Methods *163*, 161–175.

766 Martorell, A.J., Paulson, A.L., Suk, H.J., Abdurrob, F., Drummond, G.T., Guan, W., Young, J.Z.,
767 Kim, D.N.W., Kritskiy, O., Barker, S.J., et al. (2019). Multi-sensory gamma stimulation
768 ameliorates Alzheimer's-associated pathology and improves cognition. Cell *177*, 256-271.e22.

769 Mayberg, H.S., Lozano, A.M., Voon, V., McNeely, H.E., Seminowicz, D., Hamani, C., Schwalb,
770 J.M., and Kennedy, S.H. (2005). Deep Brain Stimulation for Treatment-Resistant Depression.
771 Neuron *45*, 651–660.

772 Mazzoni, A., Lindén, H., Cuntz, H., Lansner, A., Panzeri, S., and Einevoll, G.T. (2015).
773 Computing the local field potential (LFP) from integrate-and-fire network models. PLoS Comput.
774 Biol. *11*, e1004584.

775 McIntyre, C.C., and Anderson, R.W. (2016). Deep brain stimulation mechanisms: the control of
776 network activity via neurochemistry modulation. J. Neurochem. *139*, 338–345.

777 Muldoon, S.F., Pasqualetti, F., Gu, S., Cieslak, M., Grafton, S.T., Vettel, J.M., and Bassett, D.S.
778 (2016). Stimulation-based control of dynamic brain networks. PLOS Comput. Biol. *12*,
779 e1005076.

780 Nestler, E.J., and Carlezon, W.A. (2006). The mesolimbic dopamine reward circuit in
781 depression. Biol. Psychiatry *59*, 1151–1159.

782 Pesaran, B., Pezaris, J.S., Sahani, M., Mitra, P.P., and Andersen, R.A. (2002). Temporal
783 structure in neuronal activity during working memory in macaque parietal cortex. Nat. Neurosci.
784 *5*, 805–811.

785 Pesaran, B., Vinck, M., Einevoll, G.T., Sirota, A., Fries, P., Siegel, M., Truccolo, W., Schroeder,
786 C.E., and Srinivasan, R. (2018). Investigating large-scale brain dynamics using field potential
787 recordings: analysis and interpretation. Nat. Neurosci. *21*, 903–919.

788 Price, J.L., and Drevets, W.C. (2010). Neurocircuitry of mood disorders.
789 Neuropsychopharmacology *35*, 192–216.

790 Qiao, S., Brown, K.A., Orsborn, A.L., Ferrentino, B., and Pesaran, B. (2016). Development of
791 semi-chronic microdrive system for large-scale circuit mapping in macaque mesolimbic and
792 basal ganglia systems. In Proceedings of the Annual International Conference of the IEEE
793 Engineering in Medicine and Biology Society, EMBS, (IEEE), pp. 5825–5828.

794 Rajasethupathy, P., Ferenczi, E., and Deisseroth, K. (2016). Targeting neural circuits. Cell *165*,
795 524–534.

796 Rao, V.R., Sellers, K.K., Wallace, D.L., Lee, M.B., Bijanzadeh, M., Sani, O.G., Yang, Y.,
797 Shanechi, M.M., Dawes, H.E., and Chang, E.F. (2018). Direct electrical stimulation of lateral
798 orbitofrontal cortex acutely improves mood in individuals with symptoms of depression. Curr.
799 Biol. *28*, 3893-3902.e4.

800 Rattay, F. (1999). The basic mechanism for the electrical stimulation of the nervous system.
801 Neuroscience *89*, 335–346.

802 Reinhart, R.M.G., and Nguyen, J.A. (2019). Working memory revived in older adults by
803 synchronizing rhythmic brain circuits. Nat. Neurosci. 1.

804 Rich, E.L., and Wallis, J.D. (2017). Spatiotemporal dynamics of information encoding revealed
805 in orbitofrontal high-gamma. Nat. Commun. *8*, 1139.

806 Riva-Posse, P., Choi, K.S., Holtzheimer, P.E., Crowell, A.L., Garlow, S.J., Rajendra, J.K.,
807 McIntyre, C.C., Gross, R.E., and Mayberg, H.S. (2017). A connectomic approach for subcallosal
808 cingulate deep brain stimulation surgery: prospective targeting in treatment-resistant
809 depression. Mol. Psychiatry *23*, 843–849.

810 Rosenbaum, R., Zimnik, A., Zheng, F., Turner, R.S., Alzheimer, C., Doiron, B., and Rubin, J.E.
811 (2014). Axonal and synaptic failure suppress the transfer of firing rate oscillations, synchrony
812 and information during high frequency deep brain stimulation. Neurobiol. Dis. *62*, 86–99.

813 Sani, O.G., Yang, Y., Lee, M.B., Dawes, H.E., Chang, E.F., and Shanechi, M.M. (2018). Mood
814 variations decoded from multi-site intracranial human brain activity. Nat. Biotechnol. *36*, 954.

815 Seidemann, E., Arieli, A., Grinvald, A., and Slovin, H. (2002). Dynamics of depolarization and
816 hyperpolarization in the frontal cortex and saccade goal. Science (80-.). *295*, 862–865.

817 Shewcraft, R.A., Dean, H.L., Hagan, M.A., Fabiszak, M.M., Wong, Y.T., and Pesaran, B. (2019).
818 Coherent neuronal dynamics driven by optogenetic stimulation in the primate brain. BioRxiv
819 437970.

820 Siebner, H.R., Lang, N., Rizzo, V., Nitsche, M.A., Paulus, W., Lemon, R.N., and Rothwell, J.C.
821 (2004). Preconditioning of low-frequency repetitive transcranial magnetic stimulation with
822 transcranial direct current stimulation: evidence for homeostatic plasticity in the human motor
823 cortex. J. Neurosci. *24*, 3379–3385.

824 Smith, S.M., Jenkinson, M., Woolrich, M.W., Beckmann, C.F., Behrens, T.E.J., Johansen-Berg,
825 H., Bannister, P.R., De Luca, M., Drobnjak, I., Flitney, D.E., et al. (2004). Advances in functional
826 and structural MR image analysis and implementation as FSL. Neuroimage *23*, S208–S219.

827 Solomon, E.A., Kragel, J.E., Gross, R., Lega, B., Sperling, M.R., Worrell, G., Sheth, S.A.,
828 Zaghloul, K.A., Jobst, B.C., Stein, J.M., et al. (2018). Medial temporal lobe functional
829 connectivity predicts stimulation-induced theta power. Nat. Commun. *9*, 4437.

830 Suthana, N., Haneef, Z., Stern, J., Mukamel, R., Behnke, E., Knowlton, B., and Fried, I. (2012).
831 Memory enhancement and deep-brain stimulation of the entorhinal area. N. Engl. J. Med. *366*,
832 502–510.

833 Szablowski, J.O., Lee-Gosselin, A., Lue, B., Malounda, D., and Shapiro, M.G. (2018).
834 Acoustically targeted chemogenetics for the non-invasive control of neural circuits. Nat. Biomed.
835 Eng. *2*, 475–484.

836 Tehovnik, E.J., and Slocum, W.M. (2013). Two-photon imaging and the activation of cortical
837 neurons. Neuroscience *245*, 12–25.

838 Tehovnik, E.J., Tolias, A.S., Sultan, F., Slocum, W.M., and Logothetis, N.K. (2006). Direct and
839 indirect activation of cortical neurons by electrical microstimulation. J. Neurophysiol. *96*, 512–
840 521.

841 Titiz, A.S., Hill, M.R.H., Mankin, E.A., M Aghajan, Z., Eliashiv, D., Tchemodanov, N., Maoz, U.,
842 Stern, J., Tran, M.E., Schuette, P., et al. (2017). Theta-burst microstimulation in the human
843 entorhinal area improves memory specificity. Elife *6*, e29515.

844 Tolias, A.S., Sultan, F., Augath, M., Oeltermann, A., Tehovnik, E.J., Schiller, P.H., and
845 Logothetis, N.K. (2005). Mapping cortical activity elicited with electrical microstimulation using

fMRI in the macaque. Neuron *48*, 901–911.

Tyler, W.J., Lani, S.W., and Hwang, G.M. (2018). Ultrasonic modulation of neural circuit activity. Curr. Opin. Neurobiol. *50*, 222–231.

Urdaneta, M.E., Koivuniemi, A.S., and Otto, K.J. (2017). Central nervous system microstimulation: Towards selective micro-neuromodulation. Curr. Opin. Biomed. Eng. *4*, 65–77.

Widge, A.S., Zorowitz, S., Basu, I., Paulk, A.C., Cash, S.S., Eskandar, E.N., Deckersbach, T., Miller, E.K., and Dougherty, D.D. (2019). Deep brain stimulation of the internal capsule enhances human cognitive control and prefrontal cortex function. Nat. Commun. *10*, 1536.

Williams, L.M. (2017). Defining biotypes for depression and anxiety based on large-scale circuit dysfunction: a theoretical review of the evidence and future directions for clinical translation. Depress. Anxiety *34*, 9–24.

Wu, H., Miller, K.J., Blumenfeld, Z., Williams, N.R., Ravikumar, V.K., Lee, K.E., Kakusa, B., Sacchet, M.D., Wintermark, M., Christoffel, D.J., et al. (2017). Closing the loop on impulsivity via nucleus accumbens delta-band activity in mice and man. Proc. Natl. Acad. Sci. U. S. A. 201712214.

Supplementary Information: Supplementary Information contains Supplementary Tables S1-S2 and Supplementary Figures S1-S6.

Acknowledgements: We would like to thank Baldwin Goodell, Charles Gray, Jessica Kleinbart, and Amy Orsborn for assistance with chamber and microdrive system design; Stephen Frey and Brian Hynes for custom modifications to the Brainsight system; Keith Sanzenbach and Pablo Velasco from NYU Center for Imaging for help with magnetic resonance imaging and diffusion weighted imaging; Ryan Shewcraft, John Choi, Marsela Rubiano, Yoohee Jang, Octavia Martin, and NYU Office of Veterinary Resources for help with animal preparation and care. This work was supported, in part, by the Defense Advanced Research Projects Agency (DARPA) under Cooperative Agreement Number W911NF-14-2-0043, issued by the Army Research Office contracting office in support of DARPA'S SUBNETS program (to B.P.). The views, opinions, and/or findings expressed are those of the author(s) and should not be interpreted as representing the official views or policies of the Department of Defense or the U.S. Government. This work was also supported by an award from Simons Collaboration on the Global Brain (to B.P.), and US National Institutes of Health (NIH) BRAIN grant R01-NS104923 (to B.P.).

Author Contributions: S.Q. and B.P. conceived and designed the experiment; S.Q., K.A.B., J.I.S., B.F. and B.P. performed the research; S.Q. and B.P. analyzed the data; S.Q. and B.P. wrote the manuscript. B.P. oversaw and guided all aspects of the project.

Competing Financial Interests: There are no competing financial interests.

886 **STAR METHODS**

887 **KEY RESOURCES TABLE**

REAGENT or RESOURCE	SOURCE	IDENTIFIER
Software and Algorithms		
Custom code and algorithms in MATLAB	This paper	N/A
Experimental hardware		
Microelectrodes (recording)	Alpha Omega single electrodes	http://www.ao-neuro.com/index.php?route=product/product&path=65&product_id=63
Microelectrodes (recording and microstimulation)	MicroProbes monopolar electrodes	https://microprobes.com/products/metal-microelectrodes/monopolar-electrodes/platinum-iridium
Neural recordings and amplifier	NSpike NDAQ system, Harvard Instrumentation	http://nspike.sourceforge.net/#Overview
Microstimulator	Blackrock Microsystems CereStim R96	https://blackrockmicro.com/neuroscience-research-products/ephys-stimulation-systems/cerestim-96-neurostimulation-system/
Stim-record headstages	Blockrock Microsystems	https://blackrockmicro.com/neuroscience-research-products/ephys-headstages/analog-headstages/

888

889 **EXPERIMENTAL PROCEDURES**

890 **Large-scale microdrive system design**

891 We developed a customized large-scale semi-chronic microdrive system for mapping and
892 manipulating large-scale network dynamics. The screw-driven actuation mechanism of the
893 microdrive provides bi-directionally independent control of the position of 220 microelectrodes
894 (1.5-mm spacing) along a single axis with a range up to 32 mm (Monkey M) and 40 mm (Monkey
895 A) with 125-μm pitch (Dotson et al., 2017). Each actuator consists of a lead screw, a teardrop
896 brass shuttle bonded to the electrode tail with conductive epoxy, and a compression spring. Each
897 electrode can be moved with an accuracy of approximately 15 μm. For Monkey M, we distributed
898 two types of microelectrode in the microdrive, 160 platinum/iridium (Pt/Ir) electrodes
899 (MicroProbes, Gaithersburg, MD) with impedance 0.1–0.5 MΩ for extracellular recording and
900 microstimulation, and 60 tungsten electrodes (Alpha Omega, Israel) for extracellular recording

901 with impedance 0.8–1.2 MΩ. For Monkey A, we loaded 220 Pt/Ir electrodes (MicroProbes,
902 Gaithersburg, MD) with impedance 0.5 MΩ for extracellular recording and microstimulation.
903 Electrode impedances were measured at 1 kHz (Bak Electronics, Umatilla, FL). The tungsten
904 electrode's shank diameter was 125 μm and its total diameter was 250 μm with glass insulation.
905 The Pt/Ir electrode's shank diameter was 225 μm and its total diameter was 304 μm with
906 parylene C and polyimide insulation.
907
908 **Magnetic resonance imaging and processing**
909 We reconstructed each monkey's brain, skull and cerebral vasculature (Brainsight®, Rogue
910 Research, Montreal, QC) from anatomical magnetic resonance images (MRIs) and MRIs using
911 ABLAVAR® contrast agent for angiography with a T1-weighted magnetization-prepared rapid
912 acquisition gradient-echo (MPRAGE) sequence. We also performed multishell high-angular
913 resolution diffusion imaging (HARDI) tractography (Jbabdi et al., 2012) registered to microdrive
914 implantation. We collected diffusion weighted images to reconstruct white matter tracts
915 connecting key cortical and subcortical areas of interest. During MRI procedures, the monkeys
916 were anesthetized with isoflurane and placed in the scanner in sphinx position. We acquired data
917 with a 3-Tesla (3T) Siemens Allegra (Erlangen, Germany) using 3 elements out of a 4-channel
918 phased array from Nova Medical Inc. (Wilmington, MA) and 64 gradient directions in 1.2 mm^2 in-
919 plane resolution (TR = 7000 ms; TE = 110 ms; b-values: 0, 750, 1500, 2250 s/mm^2; FOV: 80×64
920 pixels; slices: 48; slice thickness: 1.2 mm; DWI to b_0 ratio 65:1). To correct for geometric
921 distortions from field inhomogeneities caused by the non-zero off-resonance fields, we collected
922 data with reversed phase-encode blips, forming pairs of images with distortions going in opposite
923 directions. From these pairs, we estimated the susceptibility-induced off-resonance field using
924 FSL's TOPUP tool (Smith et al., 2004). We combined the two images into a single corrected
925 image. We corrected Eddy currents generated by the 64 gradient directions using FSL's eddy
926 tool (Andersson and Sotiropoulos, 2015).

927

928 **Experimental preparation**

929 All surgical and experimental procedures were performed in compliance with the National
930 Institute of Health Guide for Care and Use of Laboratory Animals and were approved by the New
931 York University Institutional Animal Care and Use Committee. Two male rhesus macaques
932 (*Macaca mulatta*) participated in the study (Monkey M, 8.4 kg and Monkey A, 7 kg at the
933 beginning of the experiments). We performed a craniotomy and dura thinning on the targeted
934 brain regions over the left (Monkey M) and right (Monkey A) hemispheres. We implanted a
935 customized large-scale recording chamber (Gray Matter Research, Bozeman, MT) fitted to the
936 skull surface using MR-guided stereotaxic surgical techniques (Brainsight®, Rogue Research,
937 Montreal, QC) (Qiao et al., 2016). We aligned the chamber and registered it within 1 mm of the
938 target coordinates (nominally 0.4 mm) and affixed and sealed it to the skull surface via C&B-
939 METABOND® (Parknell Inc., Edgewood, NY) and dental acrylic. We then mounted the microdrive
940 into the chamber and sealed it with compressed gaskets and room-temperature-vulcanizing
941 (RTV) sealant (734 flowable sealant, Dow Corning, Midland, MI). To limit damage to the
942 vasculature, midline, and ventricles when lowering electrodes, we only advanced a subset of
943 electrodes along trajectories considered safe, greater than 2 mm from MR-visible vasculature,
944 ventricles, and midline.

945

946 **Neural recordings and microstimulation**

947 The monkeys were awake, head-restrained and seated in a primate chair placed in an unlit
948 sound-attenuated electromagnetically shielded booth (ETS Lindgren). Neural recordings were
949 referenced to a ground screw implanted in the left posterior parietal lobe (Monkey M) and left
950 occipital lobe (Monkey A), respectively, with the tip of the screw just piercing through the dura
951 mater. Neural signals from all channels were simultaneously amplified and digitized at 30 kHz
952 with 16 bits of resolution with the lowest significant bit equal to 0.1 μV (NSpike, Harvard

953 Instrumentation Lab; unit gain headstage, Blackrock Microsystems), and continuously streamed
954 to disk during the experiment with lights switched off in the recording booth.
955
956 We applied microstimulation using a bipolar configuration, made by simultaneously
957 sending a biphasic charge-balanced square wave pulse via a pair of Pt/Ir microelectrodes with
958 the same pulse amplitude, pulse width, and interphase interval, but opposite polarity (e.g.
959 cathode-lead for electrode 1 and anode-lead for electrode 2) (Cerestim R96, Blackrock
960 Microsystems, Salt Lake City, UT). We used the pulse width as 100 μs per phase and
961 interphase interval as 53 μs for all stimulation sessions. The Pt/Ir microelectrodes had a typical
962 tip geometric surface area of 223 ± 37 μm^2. For instance, a single pulse, with amplitude of 40
963 μA and width of 100 μs per phase (4 nC/ph), could yield a charge density of approximately 1800
964 $\mu C/cm^2$. We simultaneously recorded neural signals from all electrodes while stimulating at
965 certain pair of electrodes. No seizure activity due to stimulation was detected during
966 experiments.
967
968 We implemented two microstimulation protocols to perform causal network analysis.
969 Primarily used in this study, we designed a novel multisite spatiotemporal patterned
970 microstimulation framework to assess changes in the weight of network edges identified using
971 evoked LFP responses to single microstimulation pulses. For each stimulation bout, the
972 stimulation pattern started with a Pre-tetanic single microstimulation pulse from a pair of
973 electrodes at a network site (sender) to identify the network edges, followed by a TetMS from
974 another pair of electrodes at another network site (modulator), and followed by a Post-tetanic
975 single microstimulation pulse at the sender. The latency between the Pre-tetanic pulse and the
976 onset of the TetMS (τ_{Pre}) was either 0.5 or 1 s. The duration (T) of the TetMS pulse train and the
977 latency (τ_{Probe}) between the offset of TetMS pulse train and the onset of Post-tetanic single pulse
978 varied in a pseudo-random fashion bout by bout (T: range = 50-2000 ms; τ_{post}: range = 0-200

979 ms; mean: 57 ms; and median: 50 ms; see **Table S1**). We also varied the inter-trial interval trial
980 by trial (duration of each stimulation bout plus 2-4 s variation). We summarized all stimulation
981 parameters in **Table S1**. We defined the edge weight of identified network edges as the peak
982 magnitude of pulse-triggered averaged evoked LFP response within a 100-ms post single-pulse
983 epoch.
984
985 We also used a single-pulse microstimulation protocol using either periodic or Poisson
986 pulse train (Shewcraft et al., 2019) to identify network edges. This protocol consisted of 1-s
987 pulse trains and 1-3 s baseline epochs. Due to stimulation artifact, to preserve a minimum 100-
988 ms post single-pulse epoch for analyzing the response to each of pulses, we used pulse train
989 frequencies of 5 and 10 Hz with corresponding refractory period of 200 and 100 ms,
990 respectively.
991
992 Of 266 stimulation site-amplitude combinations tested to establish the threshold
993 microstimulation, 16 site-amplitude combinations revealed 78 significant functional interactions
994 between the sender and receiver in 21 network edges. The established threshold for single
995 pulses ranged from 10 to 100 μA with a median amplitude of 40 μA (**Table S1**).
996
997 **QUANTIFICATION AND STATISTICAL ANALYSIS**
998 **Estimation of sampled brain network nodes and edges**
999 We consider each brain region to be a network node. We sampled each node by positioning an
1000 electrode at a site in the node. For every pair of electrodes that simultaneously recorded activity
1001 in two nodes, we obtained one sample of the network edge connecting the two nodes.
1002 Repeated node sampling enabled repeated edge sampling. With M electrodes positioned at
1003 different sites in Node1, and N less than M electrodes in Node2, we obtained N non-overlapping
1004 samples of the Node1-Node2 network edge. In Monkey M, we sampled four cortical nodes at

1005 3521 sites (1506 OFC, 890 ACC, 817 PFC, and 308 M1 sites) and three subcortical nodes at
1006 1125 sites (915 CN, 122 Put, and 88 GP sites). In Monkey A, we sampled seven cortical nodes
1007 at 3900 sites (319 OFC, 469 ACC, 343 PCC, 427 PFC, 713 M1, 429 S1, and 1200 PPC sites)
1008 and eight subcortical nodes at 997 sites (614 CN, 214 Put, 59 GP, 45 Amyg, 25 PrS, 20 SI, 2
1009 BFB, and 18 NAc). We targeted our causal network analysis to 9548 samples from the cortico-
1010 subcortical limbic network across two monkeys, specifically for 1359 OFC-ACC, 1244 OFC-
1011 PFC, 1529 OFC-CN, 336 OFC-Put, 45 OFC-Amyg, 1244 ACC-PFC, 1359 ACC-CN, 336 ACC-
1012 Put, 45 ACC-Amyg, 1244 PFC-CN, 336 PFC-Put, 45 PFC-Amyg, 336 CN-Put, 45 CN-Amyg,
1013 and 45 Put-Amgy interactions.
1014

1015 **Pulse-triggered evoked potentials**

1016 We obtained LFP activity offline by low-pass filtering the broadband raw recording at 400 Hz
1017 using a multitaper filter with time duration of 0.025 s, frequency bandwidth of 400 Hz, and center
1018 frequency of 0 Hz, and then down-sampled to 1 kHz from 30 kHz. To limit the common-mode
1019 confounds of the neural recordings, we digitally referenced the neural signal of each channel to
1020 its nearest neighbor within 3 mm based on the electrode depth. We removed the events from
1021 the analysis if they exceeded 10 standard deviations of from the mean across the stimulation
1022 event pool. We also removed noisy or bad channels via visual inspection. Pulse-triggered
1023 evoked potentials were computed by averaging LFPs aligned to the onset time of each single
1024 pulse. The z-scored pulse-triggered evoked potentials were then computed using the standard
1025 deviation (SD) of the baseline (-30 to -5 ms). We computed the baseline SD for each electrode
1026 separately using all time points in the baseline window of the pulse-triggered evoked potential.
1027

1028 **Pulse-triggered multiunit activity**

1029 We obtained multiunit activity (MUA) offline by first band-pass filtering the broadband raw
1030 recording from 0.3 to 6.6 kHz with time duration of 0.01 s, frequency bandwidth of 3 kHz, and

1031 center frequency of 3.3 kHz. We then applied a 3.5 standard deviation threshold to identify
1032 putative spikes (1.6-ms duration). We labeled all waveforms that exceeded this peak as
1033 multiunit action potentials. We computed multiunit peristimulus time histograms (PSTH) by
1034 aligning MUA to the onset time of each single pulse. Individual spikes were collected in 1 ms
1035 bins and the corresponding histogram was smoothed by convolving with a Gaussian function
1036 with a standard deviation of 5 ms. Data from -1 ms to 5 (or 10) ms around the single pulse onset
1037 were not used for multiunit activity analysis due to stimulation artifact.
1038
1039 **Detection of pulse-evoked LFP responses using stimAccLLR model**
1040 To quantify the detection of evoked responses to microstimulation on a single-pulse basis, we
1041 used the stimulation-based accumulating log-likelihood ratio (stimAccLLR) method to determine
1042 when selectivity in the LFP activity for the null and alternative hypotheses emerged, i.e. the
1043 latency of a stimulation response. The latency from single microstimulation pulses was
1044 determined by the time at which Pulse Event reached a detection threshold. The threshold was
1045 selected based on a trade-off between speed (latency) and accuracy (probability of correct
1046 classification) as we increased the level of the detection thresholds from AccLLR equal to zero
1047 (**Figure S4**).
1048
1049 In the stimAccLLR method, we defined a probabilistic model of the LFP activity for the
1050 two alternatives being tested. To determine the latency for a response to single microstimulation
1051 pulses, we define the two alternative hypotheses into “condition 1” and “condition 2”, where
1052 “condition 1” represents the LFP activity (Pulse Event) in the post-stimulus epoch, while
1053 “condition 2” represents LFP activity (Pulse Null) in the pre-stimulus epoch. We performed
1054 stimAccLLR on all stimulation response to single microstimulation pulses, combining all Pre-
1055 tetanic single pulses using the multisite spatiotemporal patterned microstimulation protocol and
1056 all the single pulses using the Poisson burst microstimulation protocol. For Pre-tetanic single

pulses, Pulse Event was the 100-ms LFP activity after Pre-tetanic pulse onset plus 5 or 10-ms blanking epoch due to stimulation artifact, while Pulse Null was the 100-ms LFP activity before Pre-tetanic pulse onset. For single pulses in the Poisson burst, Pulse Event was the 50-ms LFP activity after each pulse onset plus 5 or 10-ms blanking epoch due to stimulation artifact, while Pulse Null was the 50-ms LFP activity before each pulse onset.

We modeled LFP activity as independent observations from an underlying Gaussian distribution. The signal $x(t)$ at time t is expressed as a mean waveform $\mu(t)$ with additive Gaussian noise, $\varepsilon(t)$

$$x(\mathrm{t}) = \mu(t) + \varepsilon(t)$$

The likelihood of observed data $x(t)$ being generated by each model was given by

$$P[x(t) - \mu(t)|\sigma^2] \sim N(0, \sigma^2)$$

The likelihood ratio, $LLR(t)$, at time t for two time-varying Gaussian LFP models, assuming the noise in both models had the same variance, σ^2, was given by

$$LLR(t) = \log\frac{P[x(t) - \mu_1(t)|\sigma^2]}{P[x(t) - \mu_2(t)|\sigma^2]} = \frac{(x(t) - \mu_2(t))^2 - (x(t) - \mu_1(t))^2}{2\sigma^2}$$

Finally, we calculated the accumulated log-likelihood ratio by summing log-likelihoods over time:

$$AccLLR(t) = \sum_{t'=0}^{t} LL(t')$$

To quantify signal selectivity, we performed a receiver-operating characteristic (ROC) analysis on the AccLLR values. Analysis was performed every millisecond to discriminate activity from “condition 1” and “condition 2” events. We defined overall signal selectivity as the choice probability from the ROC analysis at the end of a 100-ms or 50-ms accumulation interval. We summarized the detectable frequency of the stimulation response to a single microstimulation pulses between brain regions. We run a binomial test at the significant level of

0.05 to determine if some causally sampled network edges that showed significant directed functional interactions were more likely selective than others.

Identifying modulators using intrinsic network dynamics

To identify modulators for each of identified network edges, we grouped the Pre-tetanic single pulse baseline LFP activity (500-ms epoch before pulse onset) of all sampled sites into two categories based on 'Hit' and 'Miss' trials detected from the stimAccLLR procedure. We estimated the power spectral density (PSD) of pre-pulse baseline LFP activity using multitaper methods with 500-ms sliding window with ±2-Hz smoothing. We removed the events from the analysis if they exceeded 10 standard deviations of from the mean across the stimulation event pool. We then performed the ROC analysis to test if the respective LFP power of each recorded site in 'Hit' events was significantly different from 'Miss' events in frequency bands of θ (4-7 Hz), β (14-30 Hz), and γ (32-60 Hz), respectively. We defined the recording site in the gray matter with the area under ROC curve (AUC) greater than a threshold as modulators that significantly modulated pulse-triggered stimulation responses in different frequency bands, where the threshold was set when AUC was 95% confidence interval (one-tailed test) above chance. We focused on this analysis using the data collected in the multisite spatiotemporal patterned microstimulation framework.

Spectrogram of modulator baseline intrinsic neural activity

To test whether the baseline intrinsic activity of tested modulators significantly modulated stimulation responses at the receiver, we first sorted the events by detected 'Hit' and 'Miss' events. We then estimated spectrograms of modulator intrinsic LFP activity (1-s epoch before Pre-tetanic single pulse onset) in 'Hit' and 'Miss' events, respectively, using multitaper methods with 500-ms sliding window with ±5-Hz smoothing and 5-ms stepping between spectral estimates. We tested the difference in LFP power between 'Hit' and 'Miss' events against a null

1106 hypothesis that there was no LFP power difference using a permutation test (10,000
1107 permutations). To generate the null distribution for no LFP power difference, we randomly
1108 shuffled the order of combined 'Hit' and 'Miss' events, followed by computing shuffled LFP
1109 power difference between 'Hit' and 'Miss' events. For the significant regions presented in the
1110 spectrograms ($p < 0.05$, two-tailed test), we applied a cluster correction to correct for multiple
1111 comparisons at the significant level of 0.05 (Maris et al., 2007).
1112
1113 **Correlation analysis of intrinsic neural dynamics**
1114 To examine the relationship of intrinsic neural dynamics between the modulator, sender, and
1115 receiver, we performed Spearman's rank correlation analysis using the baseline LFP activity
1116 (500-ms epoch before Pre-tetanic single pulses) at the significant level of 0.05 (modulator vs
1117 sender; modulator vs receiver).

Figure 1

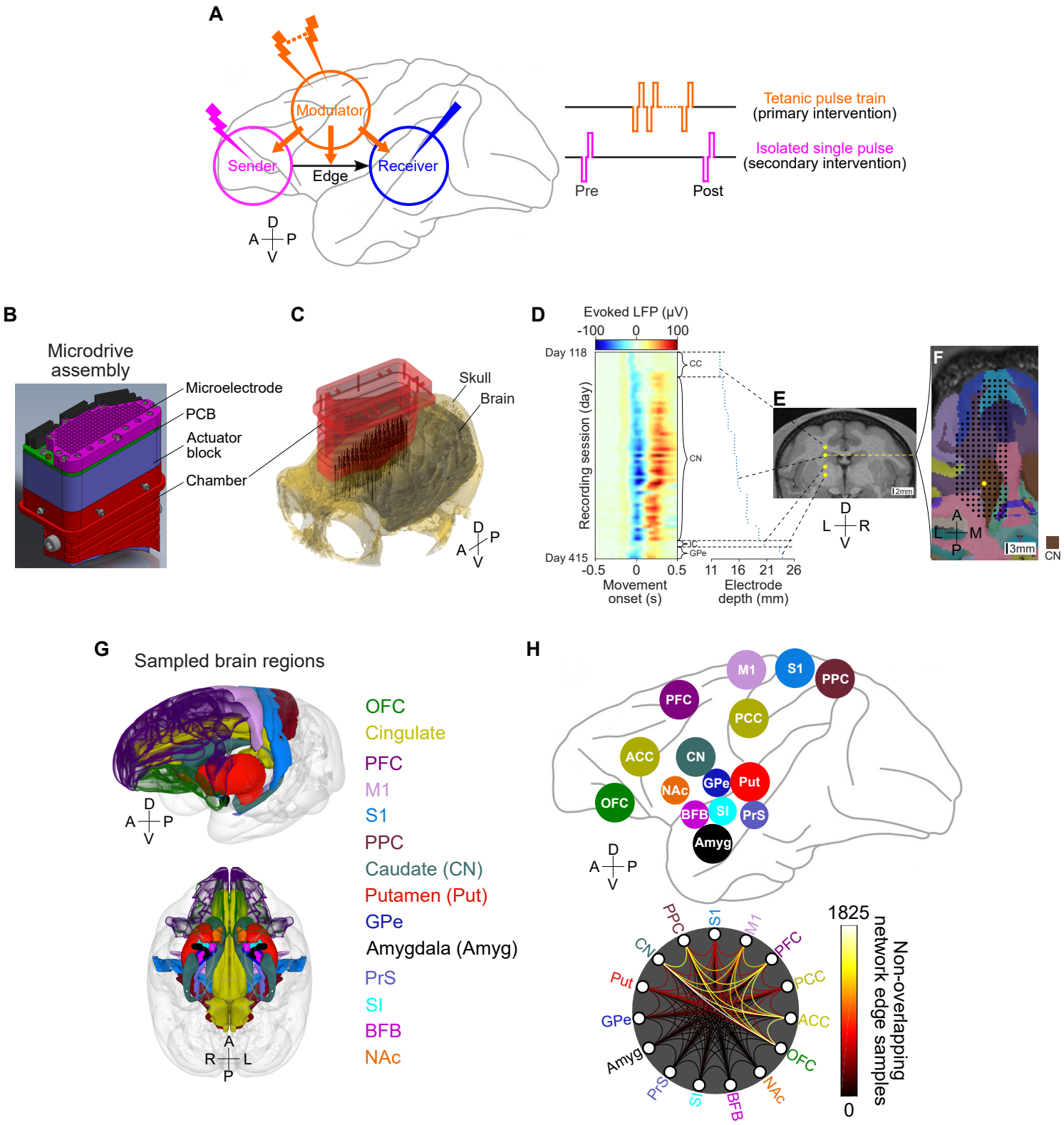
A
Modulator
Sender
Edge
Receiver
D
A
P
V
Tetanic pulse train
(primary intervention)
Isolated single pulse
(secondary intervention)
Pre
Post
B
Microdrive
assembly
Microelectrode
PCB
Actuator
block
Chamber
C
Skull
Brain
D
A
P
V
D
Evoked LFP (μV)
-100
0
100
Day 118
Day 415
Recording session (day)
CC
CN
GPe
-0.5
0
0.5
Movement
onset (s)
11
16
21
26
Electrode
depth (mm)
E
2mm
D
L
R
V
F
A
L
M
P
3mm
CN
G
Sampled brain regions
D
A
P
V
A
R
L
P
OFC
Cingulate
PFC
M1
S1
PPC
Caudate (CN)
Putamen (Put)
GPe
Amygdala (Amyg)
PrS
SI
BFB
NAc
H
M1
S1
PPC
PFC
PCC
ACC
CN
NAc
GPe
Put
OFC
BFB
SI
PrS
Amyg
D
A
P
V
PPC
S1
M1
PFC
PCC
ACC
OFC
NAc
BFB
SI
PrS
Amyg
GPe
Put
CN
1825
0
Non-overlapping
network edge samples

Figure 2

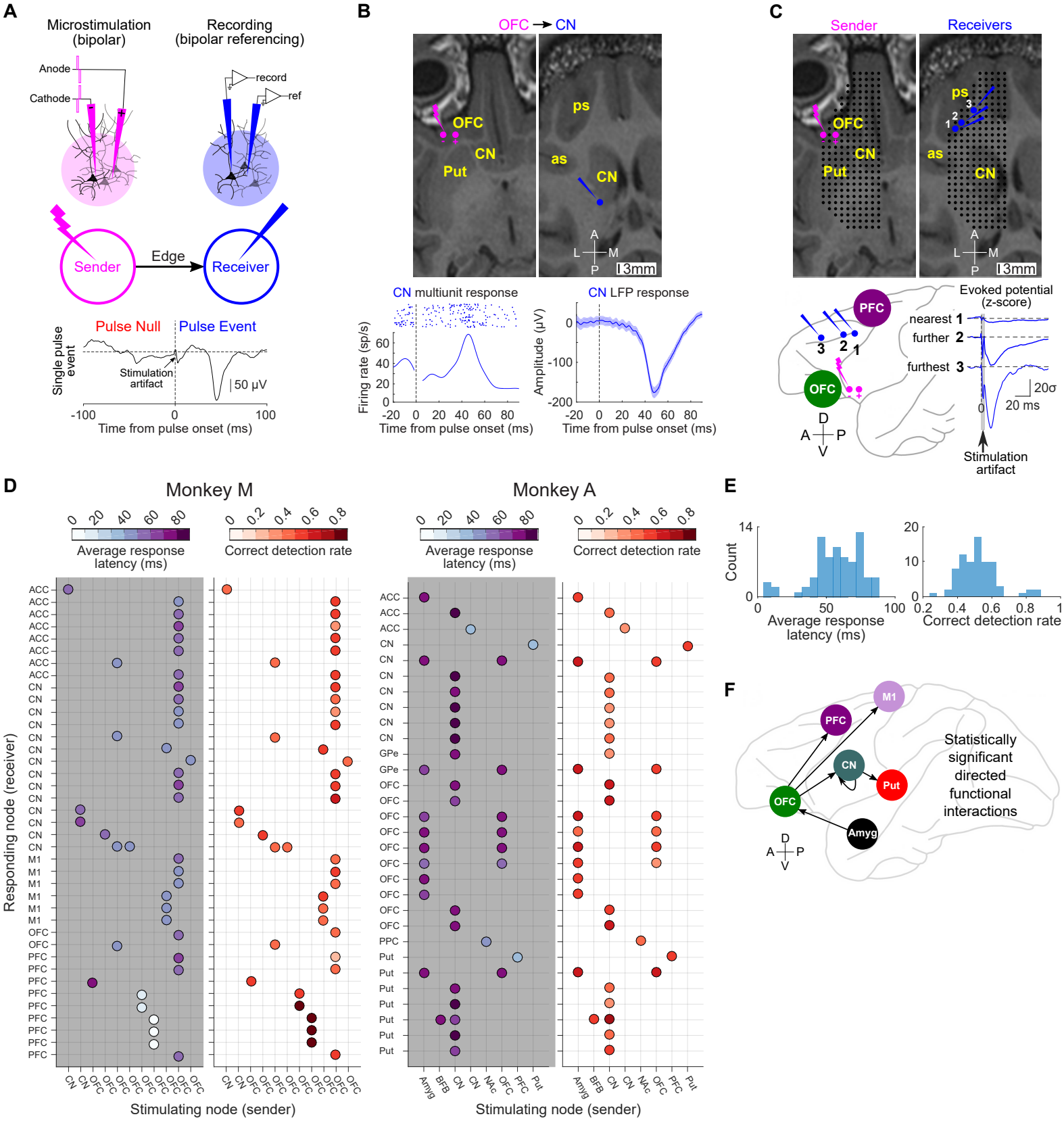
A
Microstimulation (bipolar)
Recording (bipolar referencing)
Anode
Cathode
record
ref
Sender
Edge
Receiver
Pulse Null
Pulse Event
Single pulse event
Stimulation artifact
50 µV
Time from pulse onset (ms)
B
OFC → CN
OFC
CN
Put
ps
as
3mm
CN multiunit response
CN LFP response
Firing rate (sp/s)
Amplitude (µV)
Time from pulse onset (ms)
C
Sender
Receivers
Evoked potential (z-score)
nearest 1
further 2
furthest 3
PFC
OFC
20σ
20 ms
Stimulation artifact
D
Monkey M
Monkey A
Average response latency (ms)
Correct detection rate
Responding node (receiver)
Stimulating node (sender)
E
Count
Average response latency (ms)
Correct detection rate
F
M1
PFC
CN
Put
OFC
Amyg
Statistically significant directed functional interactions

Figure 3

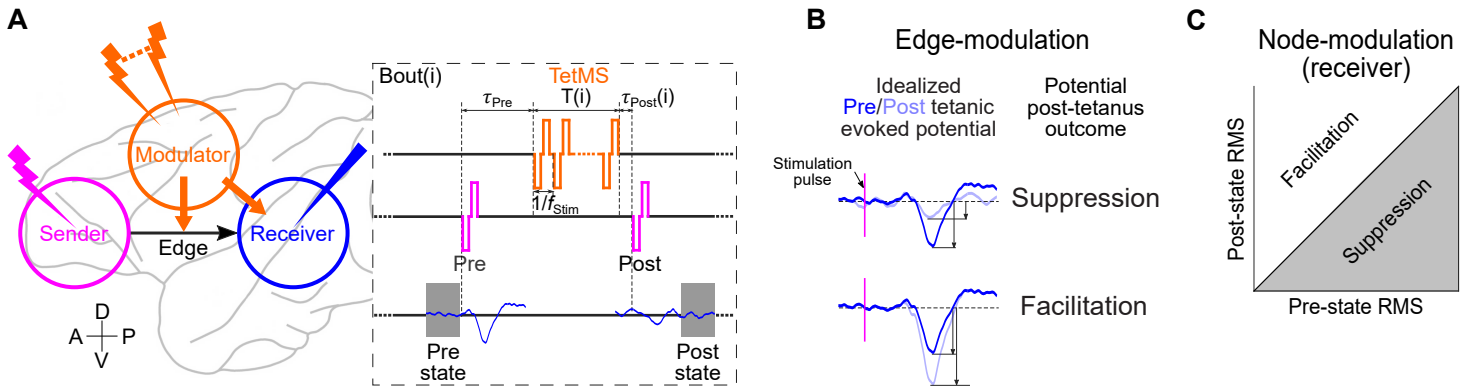
A
Modulator
Sender
Edge
Receiver
D
A
P
V
Bout(i)
TetMS
T(i)
τ_{Pre}
τ_{Post}(i)
$1/f_{Stim}$
Pre
Post
Pre state
Post state
B
Edge-modulation
Idealized Pre/Post tetanic evoked potential
Potential post-tetanus outcome
Stimulation pulse
Suppression
Facilitation
C
Node-modulation (receiver)
Post-state RMS
Pre-state RMS
Facilitation
Suppression

Figure 4

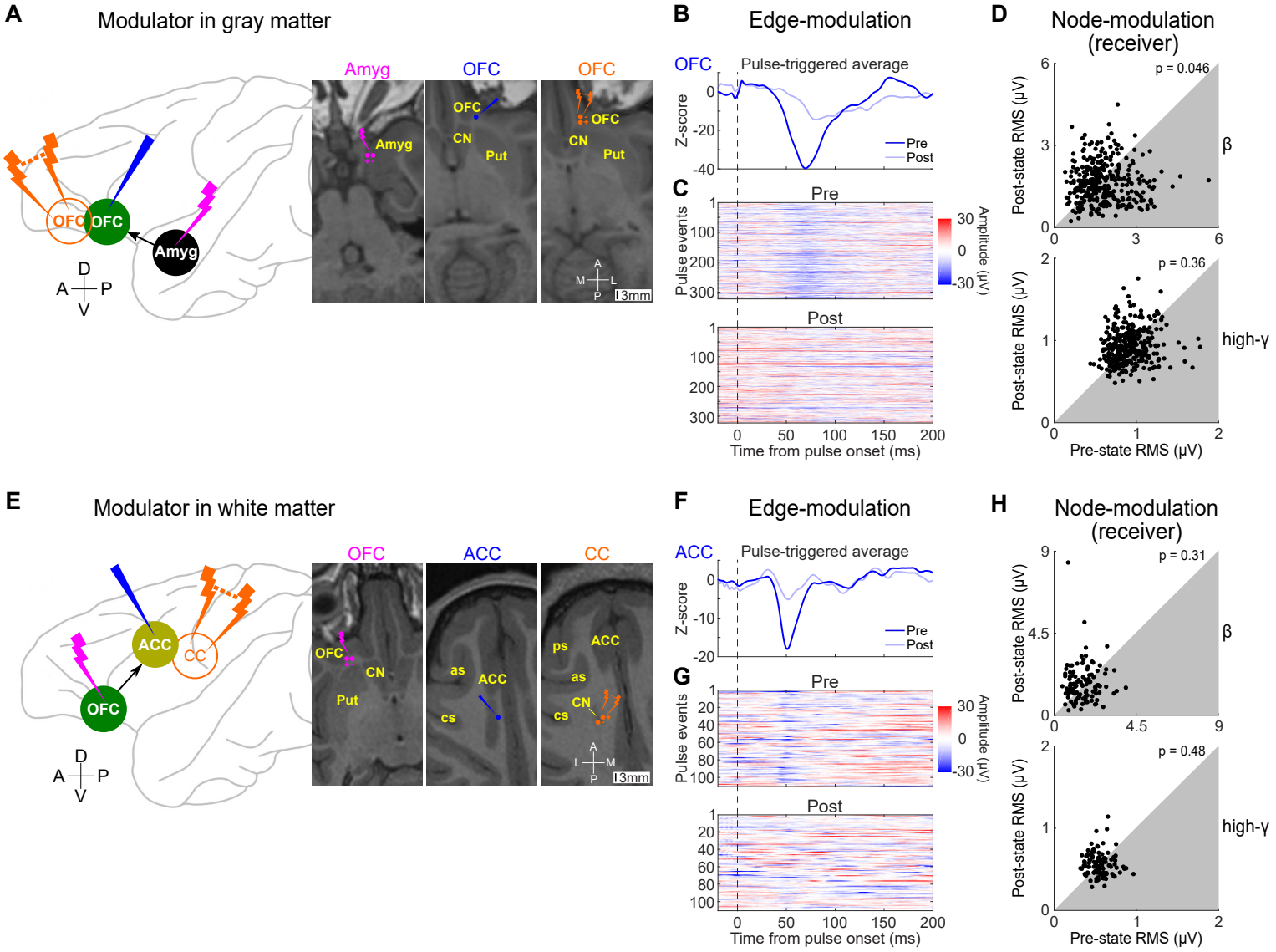
A
Modulator in gray matter
OFC
OFC
Amyg
D
A
P
V
Amyg
OFC
OFC
Amyg
OFC
CN
Put
OFC
CN
Put
A
M
L
P
3mm
B
Edge-modulation
OFC
Pulse-triggered average
Z-score
Pre
Post
C
Pre
Post
Pulse events
Amplitude (μV)
Time from pulse onset (ms)
D
Node-modulation
(receiver)
p = 0.046
β
p = 0.36
high-γ
Post-state RMS (μV)
Pre-state RMS (μV)
E
Modulator in white matter
ACC
CC
OFC
D
A
P
V
OFC
ACC
CC
OFC
CN
Put
as
ACC
cs
ps
ACC
as
CN
cs
A
L
M
P
3mm
F
Edge-modulation
ACC
Pulse-triggered average
Z-score
Pre
Post
G
Pre
Post
Pulse events
Amplitude (μV)
Time from pulse onset (ms)
H
Node-modulation
(receiver)
p = 0.31
β
p = 0.48
high-γ
Post-state RMS (μV)
Pre-state RMS (μV)

Figure 5

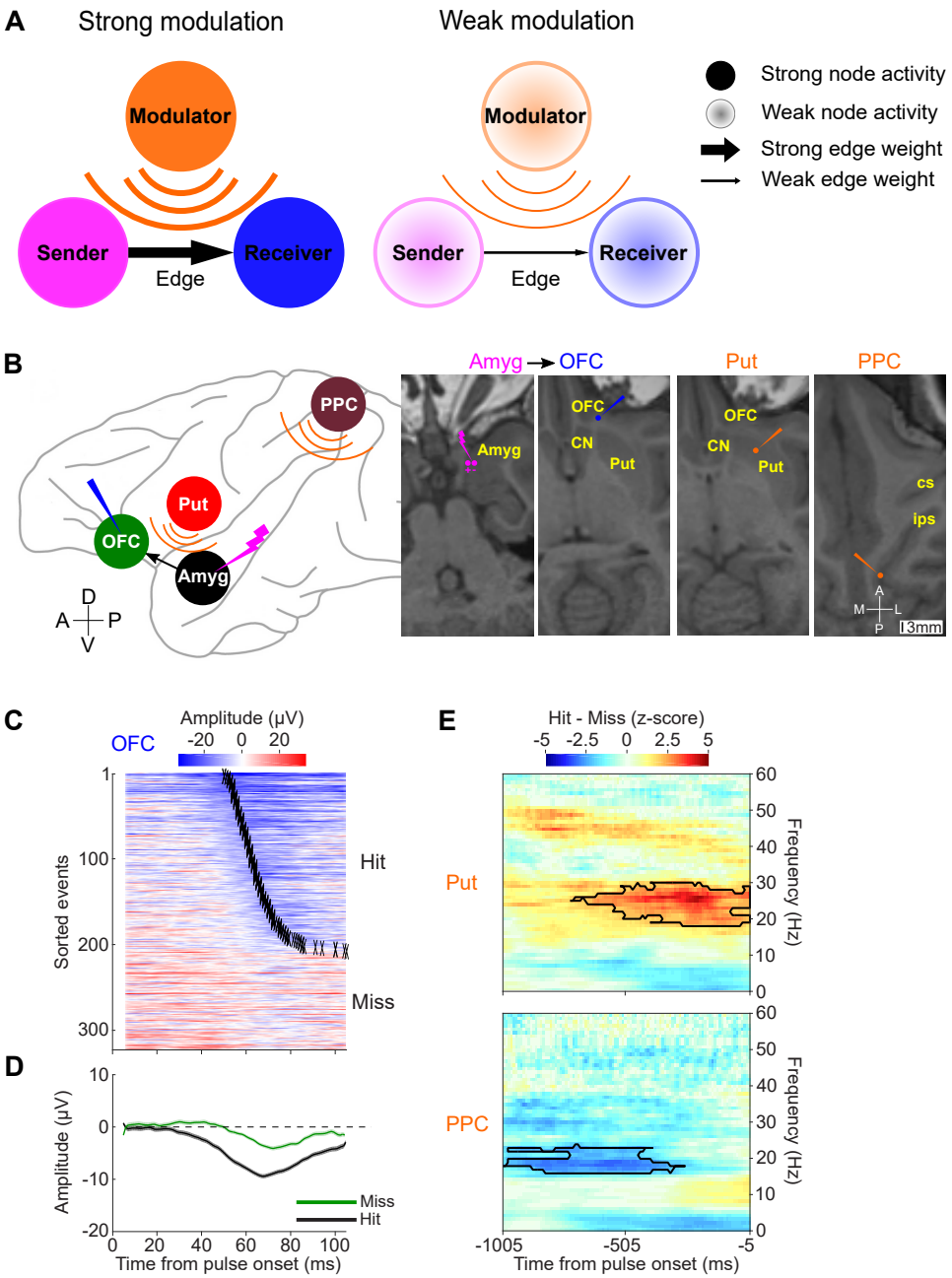
A
Strong modulation
Weak modulation
Modulator
Sender
Receiver
Edge
Strong node activity
Weak node activity
Strong edge weight
Weak edge weight
B
PPC
Put
OFC
Amyg
D
A
P
V
Amyg → OFC
Put
PPC
CN
cs
ips
M
L
13mm
C
OFC
Amplitude (μV)
-20 0 20
Sorted events
Hit
Miss
D
Amplitude (μV)
Miss
Hit
Time from pulse onset (ms)
E
Hit - Miss (z-score)
-5 -2.5 0 2.5 5
Put
PPC
Frequency (Hz)
-1005
-505
-5
Time from pulse onset (ms)

Figure S1

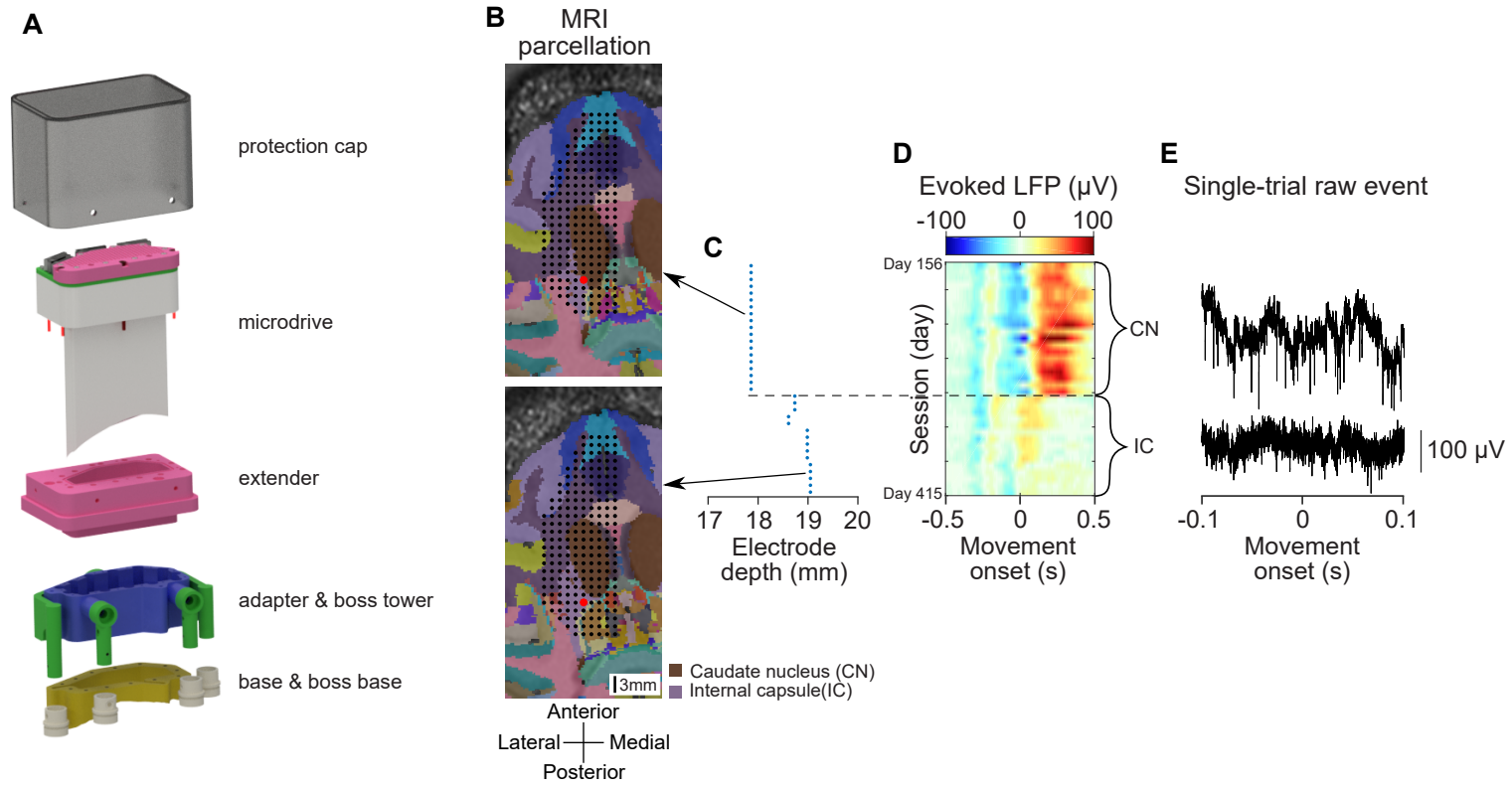

Figure S1. Using Depth Profile of Task-evoked LFP Activity Changes to Validate Anatomical Targeting, Related to Figure 1

(A) Large-scale modular implant system for simultaneous recording and manipulation in the cortico-subcortical limbic network (Monkey A).

(B) Co-registration of the electrode tracks with anatomical parcellation of white matter and grey matter of the frontal lobe of monkey M. Black dots represent the overlaid microdrive electrode grid. Red dots are the example electrode at two different horizontal MRI slice depths (top: CN, caudate nucleus; bottom: IC, internal capsule).

(C-E) Depth profile of an example electrode showing different averaged evoked LFP patterns and single-trial raw event traces in CN and IC, respectively, during the reaching epoch while the animal performed a two-alternative forced-choice task. Electrode depth was estimated from the cortical surface. Higher evoked LFPs in CN correraltes with higher spiking activity.

Figure S2

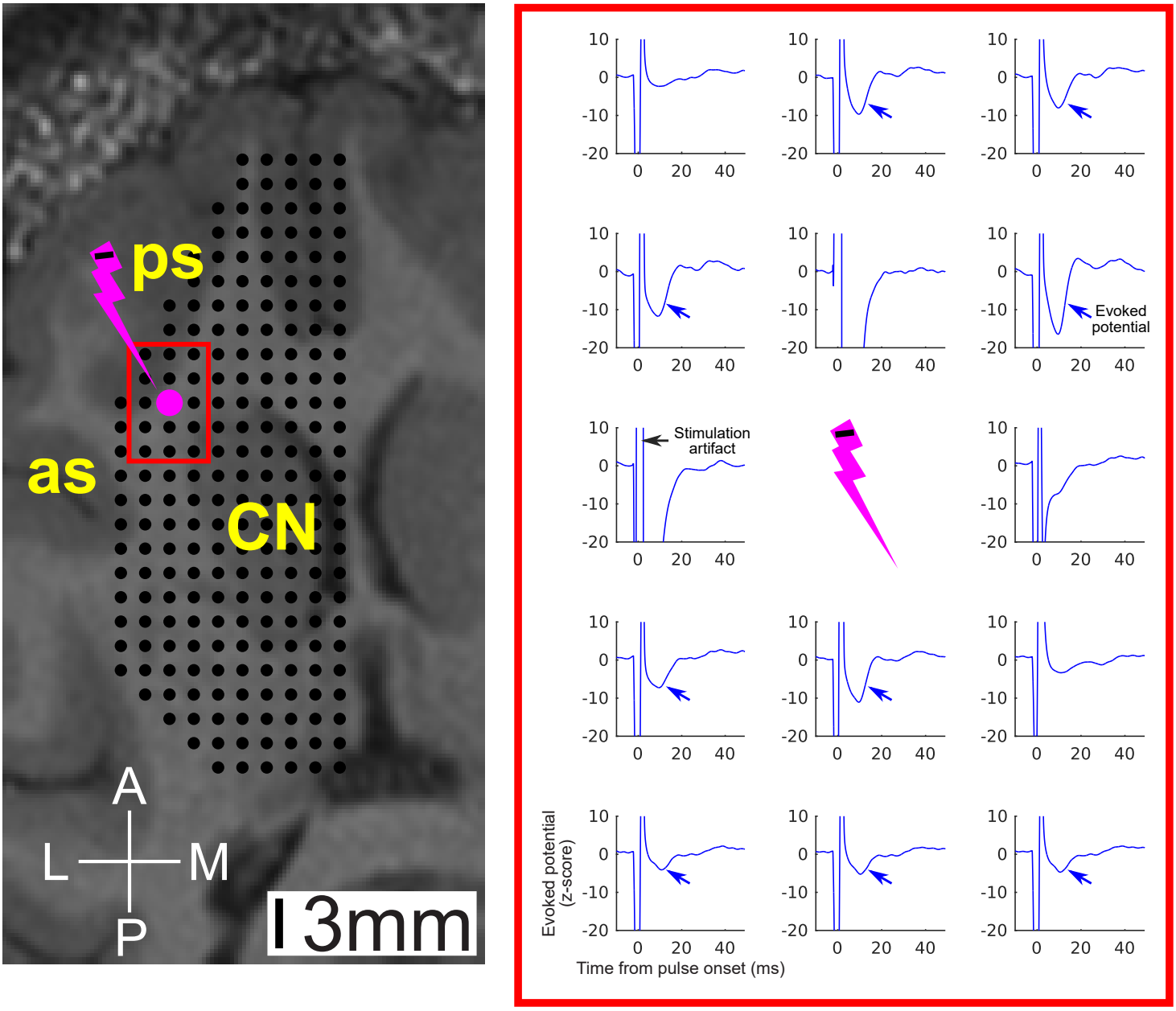

Figure S2. Pulse-triggered evoked potentials due to single, monopolar, biphasic, charge-balanced cathode-lead microstimulation pulses (40 μA, 100 μs), demonstrating stimulation responses at the near-stimulation sites might be contaminated by stimulation current spread, Related to Figure 2

CN: caudate nucleus; as: arcuate sulcus; ps: principal sulcus. Anterior (A), posterior (P), lateral (L), and medial (M) directions are indicated.

Figure S3

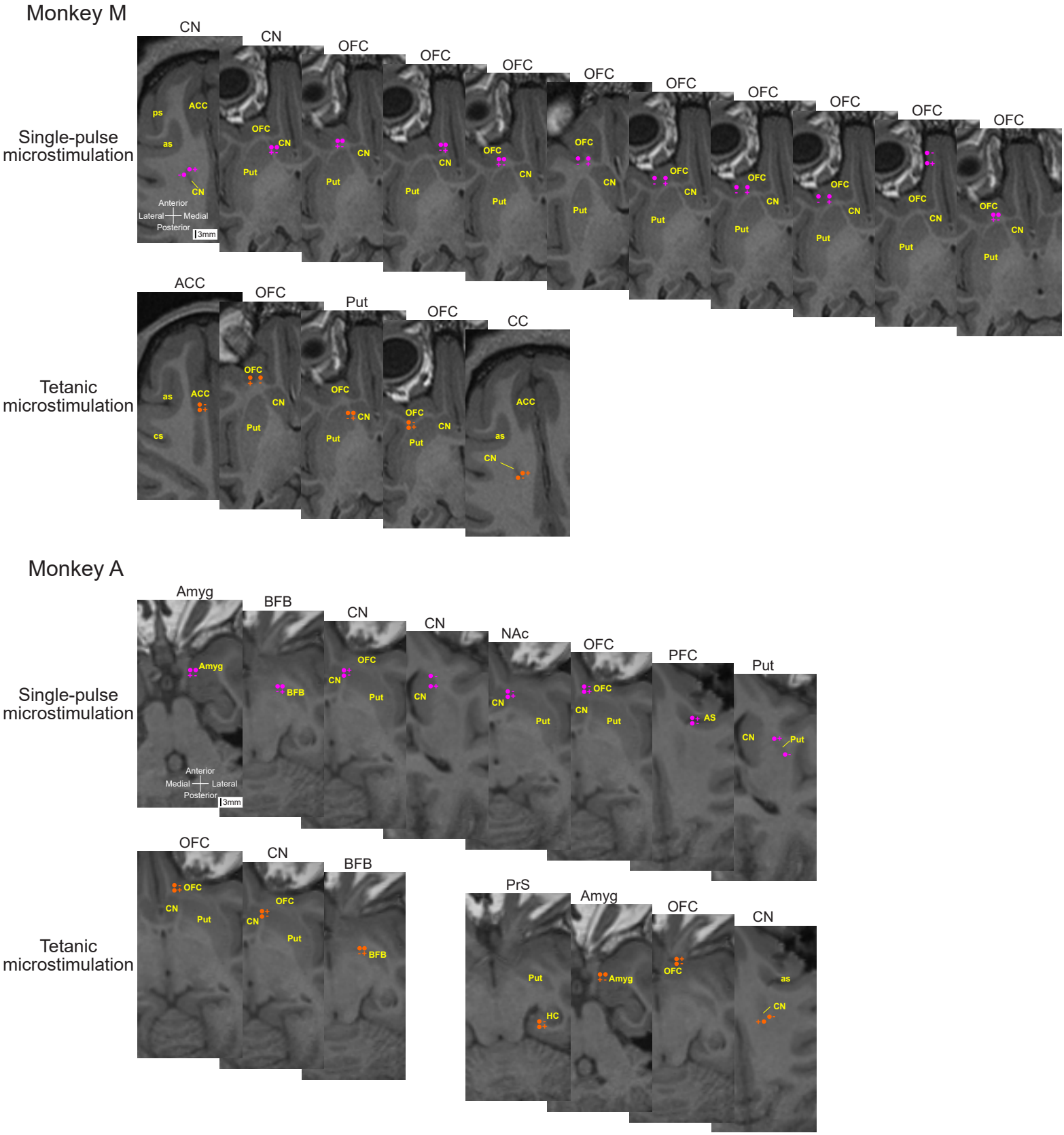

Figure S3. Anatomical locations of the single-pulse and tetanic bipolar microstimulation sites overlaid with horizontal MRI slices, Related to Figures 2, 4, and 5, and Table S1

Negative sign indicates cathode and positive sign indicates anode.

Figure S4

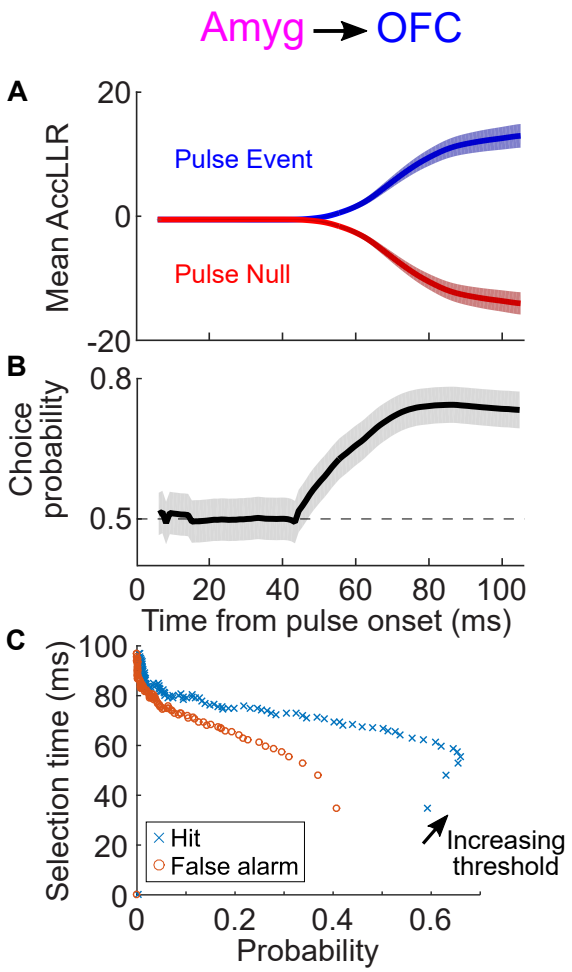

Figure S4. Identification of Network Edges Using stimAccLLR, Related to Figure 5

(A-C) The stimAccLLR results for the example network edge Amyg→OFC.

(A) Mean AccLLR of all stimulation trials during the pre-stimulus (red, Pulse Null) and post-stimulus (blue, Pulse Event) epoch (100-ms window). Error values are s.e.m., n = 322. First 5-ms data after the stimulation onset were not used due to stimulation artifact.

(B) Choice probability from the receiver-operating characteristic (ROC) analysis applied to AccLLR traces at each time bin following onset for null and event. The shaded area represents 95% confidence intervals.

(C) Probability of correctly detecting a single pulse from Pulse Event, ‘hit’ (cross), and incorrectly detecting a single pulse from Pulse Null, 'false alarm' (circle), plotted against the selection time as the level of the detection threshold is varied.

Figure S5

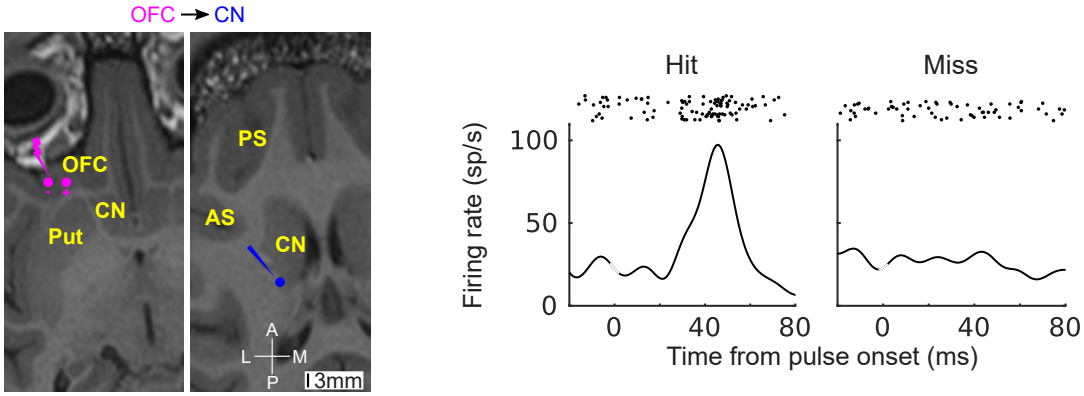

Figure S5. Comparison of driven multiunit activity of the caudate receiver between 'Hit' and 'Miss' events, Related to Figure 5

The neural activity recorded in a CN receiver was driven by single, bipolar, biphasic, charge-balanced cathode-lead microstimulation pulses (10 μA, 100 μs) delivered at an OFC sender. Driven multiunit activity are shown as raster plots and peristimulus histograms (PSTH). Error values of the driven LFP activity are s.e.m. Anterior (A), posterior (P), lateral (L), and medial (M) directions are indicated.

Figure S6

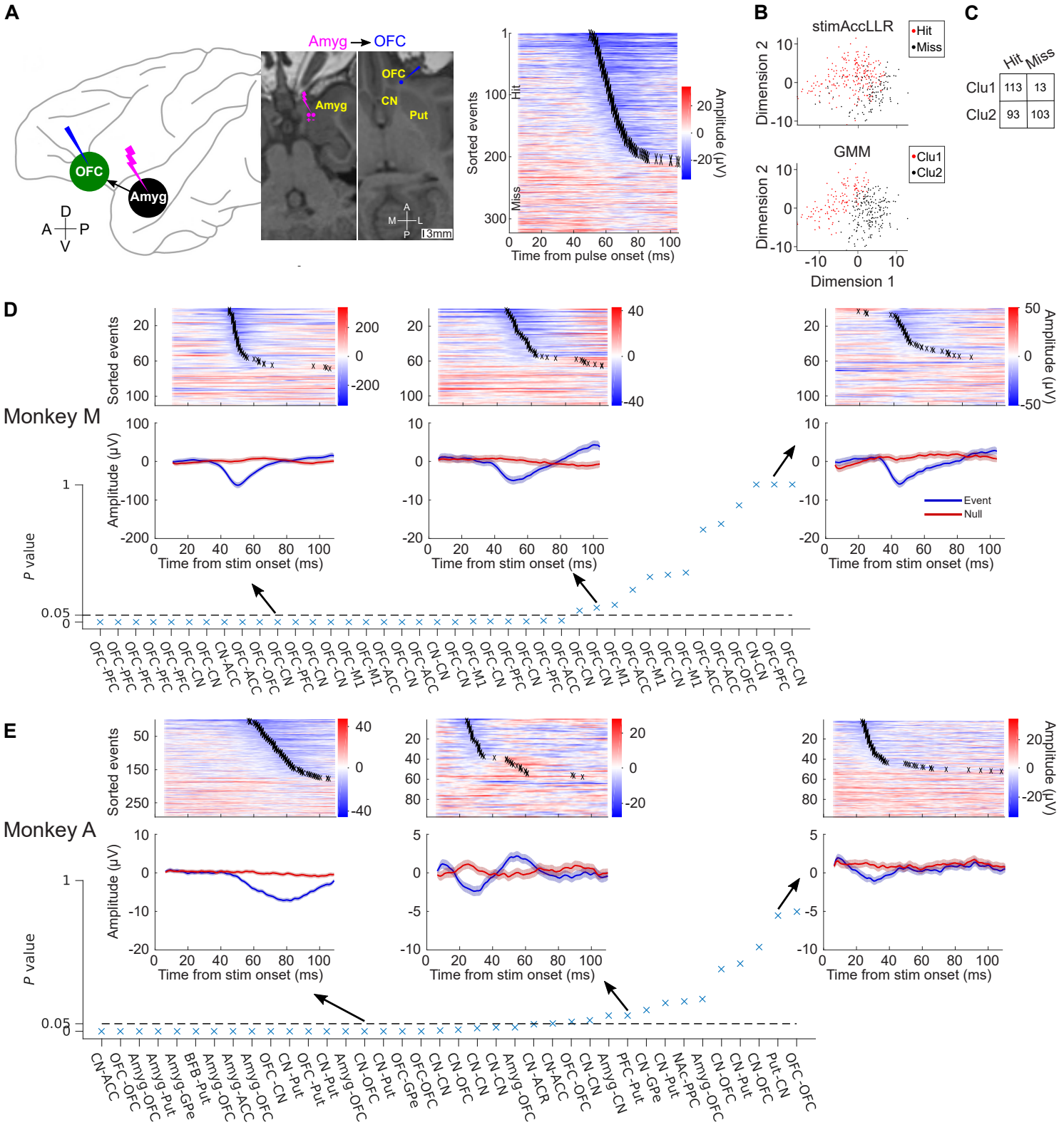

Figure S6. Fisher's Exact Test for stimAccLLR and GMM Classification Results, Related to Figure 5

(A) An example causally sampled network edge Amyg→OFC with the heat map of the pulse-by-pulse stimulation responses sorted by latencies. Anterior (A), posterior (P), lateral (L), and medial (M) directions are indicated.

(B) Cluster plots of the waveforms of Pulse Events (100-ms epoch, 5 ms after pulse onset) between the first two projected dimensions. Left: color-coded based on the stimAccLLR result showing correctly 'Hit' vs 'Miss' events; Right: color-coded using the Gaussian mixture model (GMM) classifer.

(C) Contingency table for Fisher's exact test on the data shown in (B). *P*-value of 9.05e-16 indicates that there is significant association between the classification results using AccLLR and GMM (two-tailed test, significance level = 0.05).

(D-E) P-values of all causally sampled network edges that showed directed funtional interactions and example stimAccLLR results.

Table S1. Summary of Stimulation Parameters for 78 Significant Network Edge Causal Samples, Related to Figures 2, 4, and 5, Figure S3

Single-pulse microstmulation identified causal network edge				TetMS pulse train						Edge modulation	Receiver node modulation (Median RMS comparison between Pre-state and Post-state)					
											High gamma (70-150 Hz)			Beta (10-30 Hz)		
Sender	Amp (μA)	Pulse width (μs)	Receiver	Tetanic modulator	Amp (μA)	Pulse width (μs)	Dur (ms)	Freq (Hz)	Post latency (ms)	Post-tetanic Effect	Pre-state RMS (μV)	Post-state RMS (μV)	p-val	Pre-state RMS (μV)	Post-state RMS (μV)	p-val
Multisite spatiotemporal patterned microstimulation protocol																
Amyg	40	100	ACC	OFC	30	100	50-500[a]	100	25-100[b]	Suppression	0.98	0.98	0.87	1.72	1.69	0.43
Amyg	40	100	CN	OFC	30	100	50-500	100	25-100	Suppression	1.14	1.14	0.85	1.86	1.83	0.73
Amyg	40	100	GPe	OFC	30	100	50-500	100	25-100	Suppression	2.38	2.42	0.49	6.11	5.82	0.54
Amyg	40	100	OFC	OFC	30	100	50-500	100	25-100	Suppression	1.23	1.24	0.42	1.87	1.84	0.36
Amyg	40	100	OFC	OFC	30	100	50-500	100	25-100	Suppression	0.9	0.91	0.36	**1.68**	**1.62**	**0.046**
Amyg	40	100	OFC	OFC	30	100	50-500	100	25-100	Suppression	0.83	0.83	0.87	1.09	1.01	0.088
Amyg	40	100	OFC	OFC	30	100	50-500	100	25-100	Suppression	1.67	1.59	0.24	2.77	2.67	0.15
Amyg	40	100	OFC	OFC	30	100	50-500	100	25-100	Suppression	1.27	1.26	0.53	**1.63**	**1.45**	**<0.01**
Amyg	40	100	OFC	OFC	30	100	50-500	100	25-100	Suppression	2.63	2.64	0.33	3.11	2.98	0.085
Amyg	40	100	Put	OFC	30	100	50-500	100	25-100	Suppression	0.97	0.98	0.84	2.26	2.26	0.93
BFB	60	100	Put	CN	30	100	50-500	100	25-100	Suppression	2.04	2.06	0.48	4.58	4.42	0.53
CN	20	100	ACC	ACC	40	100	250	100	20	Suppression	0.88	0.87	0.79	1.18	1.24	0.48
CN	60	100	ACC	BFB	30	100	50-500	100	25-100	Suppression	0.79	0.80	0.67	1.64	1.62	0.41
CN	60	100	CN*[#]	OFC	30	100	1000	100	50	Suppression	3.60	3.43	0.23	7.65	7.79	0.58
CN	60	100	CN*	OFC	30	100	1000	100	50	Suppression	3.63	3.46	0.19	8.37	8.73	0.35
CN	60	100	CN	BFB	30	100	50-500	100	25-100	Suppression	0.56	0.57	0.62	0.70	0.65	0.17
CN	60	100	CN	BFB	30	100	50-500	100	25-100	Suppression	0.55	0.54	0.27	0.7	0.67	0.13
CN	60	100	CN	BFB	30	100	50-500	100	25-100	Suppression	0.72	0.72	0.66	0.88	0.86	0.23
CN	60	100	CN	BFB	30	100	50-500	100	25-100	Suppression	0.46	0.48	0.27	0.77	0.75	0.45
CN	60	100	CN	BFB	30	100	50-500	100	25-100	Suppression	0.74	0.72	0.86	2.55	2.73	0.068
CN	60	100	GPe	BFB	30	100	50-500	100	25-100	Suppression	**3.94**	**4.2**	**<0.01**	4.6	4.76	0.29
CN	60	100	OFC	BFB	30	100	50-500	100	25-100	Suppression	1.98	2.01	0.59	2.23	2.09	0.22
CN	60	100	OFC	BFB	30	100	50-500	100	25-100	Suppression	1.88	1.88	0.79	2.11	1.96	0.087
CN	60	100	OFC	BFB	30	100	50-500	100	25-100	Suppression	1.37	1.37	0.79	**2.41**	**2.08**	**<0.01**
CN	60	100	OFC	BFB	30	100	50-500	100	25-100	Suppression	**2.19**	**2.48**	**<0.01**	**3.14**	**2.97**	**0.039**
CN	60	100	Put	BFB	30	100	50-500	100	25-100	Suppression	1.44	1.43	0.36	1.54	1.53	0.73
CN	60	100	Put	BFB	30	100	50-500	100	25-100	Suppression	1.31	1.31	0.90	**1.39**	**1.20**	**<0.01**
CN	60	100	Put	BFB	30	100	50-500	100	25-100	Suppression	2	2	0.74	4.55	4.22	0.16
CN	60	100	Put	BFB	30	100	50-500	100	25-100	Suppression	0.54	0.54	0.82	1.61	1.40	0.097
CN	60	100	Put	BFB	30	100	50-500	100	25-100	Suppression	**1.07**	**1**	**<0.01**	**2.91**	**2.67**	**0.014**
NAc	30	100	PPC	PrS	20	100	100-1000[c]	100	50-200	Suppression	0.76	0.75	0.67	3.89	3.7	0.26
OFC	30	100	ACC	CC	20	100	250	200	0, 50	Suppression	0.87	0.9	0.27	1.22	1.17	0.50
OFC	30	100	ACC*	CC	20	100	250	200	0, 50	Suppression	0.54	0.54	0.48	1.53	1.58	0.31
OFC	30	100	ACC	CC	20	100	250	200	0, 50	Suppression	0.82	0.79	0.18	0.44	0.49	0.38
OFC	30	100	ACC	CC	20	100	250	200	0, 50	Suppression	0.83	0.86	0.36	1.7	1.81	0.73
OFC	30	100	ACC	CC	20	100	250	200	0, 50	Suppression	2.34	2.32	0.68	2.37	2.42	0.99
OFC	30	100	ACC	CC	20	100	250	200	0, 50	Suppression	1.42	1.47	0.85	3.01	3.12	0.53
OFC	40	100	CN	Amyg	30	100	50-500	100	25-100	Suppression	1.18	1.19	0.61	1.97	1.81	0.05
OFC	30	100	CN	CC	20	100	250	200	0, 50	Suppression	**0.85**	**0.68**	**<0.01**	1.66	1.44	0.21
OFC	30	100	CN	CC	20	100	250	200	0, 50	Suppression	0.49	0.46	0.08	0.88	0.87	0.72
OFC	30	100	CN	CC	20	100	250	200	0, 50	Suppression	**3.86**	**1.73**	**<0.01**	**4.56**	**4.12**	**0.035**
OFC	30	100	CN	CC	20	100	250	200	0, 50	Suppression	0.55	0.53	0.35	0.86	0.79	0.78
OFC	30	100	CN	CC	20	100	250	200	0, 50	Suppression	1.36	1.37	0.4	2.34	2.61	0.27
OFC	30	100	CN	CC	20	100	250	200	0, 50	Suppression	0.73	0.68	0.22	1.44	1.50	0.13
OFC	30	100	CN*[#]	CC	20	100	250	200	0, 50	Suppression	6.02	5.72	0.4	19.35	21.4	0.23
OFC	100	100	CN*	OFC	100	100	1000	100	100	Suppression	2.55	2.45	0.1	8	8.06	0.64
OFC	40	100	GPe	Amyg	30	100	50-500	100	25-100	Suppression	2.40	2.41	0.94	5.94	5.84	0.60
OFC	30	100	M1*	CC	20	100	250	200	0, 50	Suppression	0.38	0.38	0.9	0.69	0.69	0.82
OFC	30	100	M1	CC	20	100	250	200	0, 50	Suppression	2.30	2.28	0.63	4-02	3.99	0.75
OFC	30	100	M1	CC	20	100	250	200	0, 50	Suppression	**4.56**	**3.92**	**<0.01**	10.79	9	0.16
OFC	40	100	OFC	Amyg	30	100	50-500	100	25-100	Suppression	0.89	0.92	0.13	**1.82**	**1.63**	**0.014**
OFC	40	100	OFC	Amyg	30	100	50-500	100	25-100	Suppression	1.66	1.63	0.39	**3.09**	**2.62**	**<0.01**
OFC	40	100	OFC	Amyg	30	100	50-500	100	25-100	Suppression	1.24	1.29	0.28	**1.62**	**1.49**	**0.011**
OFC	40	100	OFC	Amyg	30	100	50-500	100	25-100	Suppression	2.56	2.55	0.57	**3.24**	**3.02**	**0.02**
OFC	30	100	OFC	CC	20	100	250	200	0, 50	Suppression	0.46	0.45	0.4	0.55	0.49	0.17

OFC	30	100	PFC	CC	20	100	250	200	0, 50	Suppression	**5.53**	**4.46**	**<0.01**	6.47	6.29	0.43
OFC	30	100	PFC*	CC	20	100	250	200	0, 50	Suppression	0.81	0.81	0.82	1.76	1.77	0.93
OFC	30	100	PFC*	CC	20	100	250	200	0, 50	Suppression	0.75	0.78	0.35	2.09	2.05	0.74
OFC	60	100	PFC	Put	30	100	1000	100	0, 50	Bad						
OFC	40	100	Put	Amyg	30	100	50-500	100	25-100	Suppression	0.98	0.97	0.59	**2.55**	**2.25**	**0.04**
PFC	40	100	Put	OFC	30	100	250-2000[d]	100	50-200[e]	Suppression	0.95	0.94	0.16	2.16	2	0.24
Put	60	100	CN	CN	30	100	100-1000	100	50-200	Bad						
Single-pulse microstimulation protocol																
CN	40	100	ACC													
OFC	80	100	ACC													
OFC	80	100	CN*													
OFC	80	100	CN*													
OFC	50	100	CN													
OFC	30	100	CN													
OFC	10	100	CN*#													
OFC	10	100	M1*													
OFC	10	100	M1*													
OFC	10	100	M1*													
OFC	80	100	OFC													
OFC	50	100	PFC													
OFC	50	100	PFC													
OFC	50	100	PFC													
OFC	50	100	PFC													
OFC	50	100	PFC													

OFC: orbitofrontal cortex; ACC: anterior cingulate cortex; PFC: prefrontal cortex; M1: primary motor cortex; PPC: posterior parietal cortex; CN: caudate nucleus; Put: putamen; GPe: globus pallidus external; Amyg: amygdala; BFB: basal forebrain; NAc: nucleus accumbens; PrS: presubiculum; CC: corpus callosum;

[a] varied in a pseudo-random fashion (50, 100, 200, and 500 ms)
[b] varied in a pseudo-random fashion (25, 50, and 100 ms)
[c] varied in a pseudo-random fashion (100, 200, 500, and 1000 ms)
[d] varied in a pseudo-random fashion (250, 1000, and 2000 ms)
[e] varied in a pseudo-random fashion (50, 100, and 200 ms)
* Driven high gamma (70-150 Hz) activity (13 samples)
[#] Driven multiunit activity (3 samples)

Table S2. Summary of Likelihood of Detecting Stimulation Response to Single Microstimulation Pulses between Brain Regions, Related to Figure 2

		Sender node						
		OFC	**CN**	**Put**	**PFC**	**Amyg**	**BFB**	**NAc**
Receiver node	**OFC**	6/1358	4/615	0/94	0/51	6/59	0/6	0/25
	ACC	7/1165	3/507	0/93	0/93	1/97	0/12	0/53
	CN	14/1212	7/568	1/113	0/101	1/107	0/12	0/44
	Put	1/180	5/112	0/26	1/25	1/29	1/3	0/14
	GPe	1/92	1/49	0/9	0/11	1/12	0/2	0/3
	PFC	9/779	0/330	0/56	0/59	0/68	0/6	0/48
	M1	6/100	0/299	0/79	0/100	0/87	0/12	0/64
	S1	0/123	0/101	0/39	0/44	0/49	0/6	0/39
	PPC	0/403	0/18	0/115	0/149	0/136	0/18	1/403
	Amyg	0/29	0/21	0/8	0/9	0/6	0/1	0/4
	NAc	0/11	0/9	0/1	0/6	0/2		
	PrS	0/15	0/12	0/3	0/5	0/4	0/1	0/1

OFC: orbitofrontal cortex; ACC: anterior cingulate cortex; PFC: prefrontal cortex; M1: primary motor cortex; S1: primary somatosensory cortex; CN: caudate nucleus; Put: putamen; GPe: globus pallidus external; Amyg: amygdala; BFB: basal forebrain; NAc: nucleus accumbens; PPC: posterior parietal cortex; PrS: presubiculum

Data are shown as N1/N2, where N1 is the number of stimulation responding sites in each brain area and N2 is the total number of recorded sites in each brain area. Highlighted in red are statistically significant directed function interactions.